Check for updates

Ephemeris-Based Satellite Collision Rates and Probabilities

Doyle T. Hall*
Omitron, Inc., Colorado Springs, Colorado 80919

https://doi.org/10.2514/1.A36227

This study formulates a semi-analytical method to estimate statistically expected collision rates and probabilities between Earth-orbiting satellites, based on orbital state and covariance ephemeris tables. The method focuses on low-velocity interactions, for which the conjunction-by-conjunction estimation approach can be inaccurate. Comparisons to Monte Carlo simulations validate the accuracy of the calculation method. The ability to process unevenly sampled ephemerides allows application to satellites that execute frequent or continuous thrusting maneuvers. Estimating uncertainties caused by ephemeris interpolation inaccuracies enables the algorithm to detect input ephemerides with inadequate time sampling. Additionally accounting for satellite shapes and orientations requires input ephemerides that tabulate attitude information.

Nomenclature

$\mathcal{A}$ = accuracy indicator for the statistically expected number of collisions [see Eq. (34)]
$\mathcal{A}(n)$ = accuracy indicator obtained by including only every nth point of the input ephemeris tables
$\mathcal{A}_k$ = accuracy indicator for the expected number of collisions in the kth encounter segment
$\widetilde{\boldsymbol{A}}_t$ = effective relative position–position covariance at time t, adjusted to account for curvilinear trajectory effects [see Eq. (16)]
$\boldsymbol{a}_f$ = $\boldsymbol{a}_f(\boldsymbol{q})$ equals a function that calculates the 3×3 attitude matrix from the 4×1 quaternion vector $\boldsymbol{q}$
$\boldsymbol{a}_{j,t}$ = attitude matrix for the jth satellite at time t
$\widetilde{\boldsymbol{B}}_t$ = effective relative position-velocity covariance at time t, adjusted to account for curvilinear trajectory effects [see Eq. (16)]
b = bracketing ephemeris index for time t
$\boldsymbol{b}_j$ = auxiliary orbital state vector containing the jth satellite's ballistic coefficient and/or the solar radiation parameter
$\widetilde{\boldsymbol{C}}_t$ = effective relative velocity–velocity covariance, adjusted to account for curvilinear trajectory effects [see Eq. (16)]
c = closest ephemeris index for time t
$\mathbb{E}[\square]$ = statistical expectation value operator
$\boldsymbol{E}_{j,0}$ = initial equinoctial orbital element state vector for the jth satellite
e = ephemeris index
$\mathcal{F}_{t,t'}$ = collision rate integrand function at time t, calculated from satellite states and covariances provided at time t'
g = index for the iteratively refined time grid
$H(\tilde{\nu})$ = auxiliary function used to calculate average projected velocity function [see Eqs. (26) and (27)]
I_m = number of ingress events that occur during the mth Monte Carlo trial
j = satellite index; j equals 1 for the primary satellite; j equals 2 for the secondary satellite
K = total number of conjunctions, collision rate peaks, or encounter segments
k = index for conjunctions, collision rate peaks, or encounter segments
M = total number of Monte Carlo trials
M_D = mean-state Mahalanobis distance at the center of the collision sphere [equal to $(\overline{\mathcal{M}}_{0,t})^{1/2}$]
M_E = effective Mahalanobis distance at the center of the collision sphere [equal to $(\widetilde{\mathcal{M}}_{0,t})^{1/2}$]
$\overline{\mathcal{M}}_{\min,t}$ = minimum squared Mahalanobis distance over the surface of the collision sphere at time t
$\widetilde{\mathcal{M}}_{R,t}(\hat{\boldsymbol{r}})$ = squared effective Mahalanobis distance function for a point on the collision sphere at time t
M_S = minimum mean-state Mahalanobis distance over the surface of the collision sphere (equal to $[\overline{\mathcal{M}}_{\min,t}]_+^{1/2}$)
$\overline{\mathcal{M}}_{0,t}$ = squared mean-state Mahalanobis distance at the center of the collision sphere at time t
$\widetilde{\mathcal{M}}_{0,t}$ = squared effective Mahalanobis distance at the center of the collision sphere at time t
$\mathcal{N}$ = multivariate normal function [see Eq. (2)]
N_c = $N_c(\tau_a, \tau_b)$ equals the statistically expected number of collisions accumulated over the interval $\tau_a \le t < \tau_b$
N_c^{MC} = number of hits in a Monte Carlo simulation accumulated over the interval $\tau_a \le t < \tau_b$
$N_{c,k}$ = statistically expected number of collisions for the kth conjunction or the kth encounter segment
$N_{c,t}$ = statistically expected number of collisions accumulated over the time interval $\tau_a \le t' < t$
$\dot{N}_{c,t}$ = $\dot{N}_c(t)$ equals the statistically expected collision rate at time t
$\langle \dot{N}_{c,t} \rangle$ = average of the four alternate collision rate estimates
$\dot{N}_{c,t}^D$ = $\dot{N}_c^D(\boldsymbol{X}_t)$ equals the deterministic collision rate for two perfectly tracked spheres or convex hulls
$\dot{N}_{c,t}^{\mathrm{high}}$ = highest alternate collision rate estimate for the collision rate at time t
$\dot{N}_{c,t}^{(i)}$ = ith alternate estimate for the collision rate at time t; i equal to 1 is the main estimate; i equal to $1, \ldots, 4$ are the four alternate estimates
$\dot{N}_{c,t}^{\mathrm{low}}$ = lowest alternate collision rate estimate for the collision rate at time t
$N_{c,t}^{\mathrm{MC}}$ = statistically expected number of collisions estimated from the number of hits in a Monte Carlo simulation accumulated over the time interval $\tau_a \le t' < t$
N_j^e = number of time points in an ephemeris for the jth satellite
N_j^S = number of elements in the orbital state vector for the jth satellite
n = integer interval used for sampling input ephemerides
P_c = $P_c(\tau_a, \tau_b)$ equals the probability of collision accumulated over the risk assessment interval $\tau_a \le t < \tau_b$

Received 29 August 2024; accepted for publication 16 November 2024; published online Open Access 17 January 2025. Copyright © 2025 by the American Institute of Aeronautics and Astronautics, Inc. The U.S. Government has a royalty-free license to exercise all rights under the copyright claimed herein for Governmental purposes. All other rights are reserved by the copyright owner. All requests for copying and permission to reprint should be submitted to CCC at www.copyright.com; employ the eISSN 1533-6794 to initiate your request. See also AIAA Rights and Permissions www.aiaa.org/randp.

*Senior Conjunction Assessment Research Scientist, 5450 Tech Center Drive, Suite 400; doyle.hall@omitron.com (Corresponding Author).

Downloaded by 24.8.227.60 on February 14, 2025 | http://arc.aiaa.org | DOI: 10.2514/1.A36227

Downloaded by 24.8.227.60 on February 14, 2025 | http://arc.aiaa.org | DOI: 10.2514/1.A36227

$P_c^{\max}$ = upper-bound collision probability accumulated over the risk assessment interval $\tau_a \le t < \tau_b$

P_c^{MC} = probability of collision in a Monte Carlo simulation accumulated over the interval $\tau_a \le t < \tau_b$

$P_c^{\min}$ = lower-bound collision probability accumulated over the risk assessment interval $\tau_a \le t < \tau_b$

$P_{c,k}$ = probability of collision for the kth conjunction or the kth encounter segment

$P_{c,t}$ = probability of collision accumulated over the time interval $\tau_a \le t' < t$

$P_{c,t}^{\mathrm{MC}}$ = probability of collision in a Monte Carlo simulation accumulated over the time interval $\tau_a \le t' < t$

$\overline{\boldsymbol{P}}_j^{\mathrm{BI}}(t)$ = position-velocity covariance of the jth satellite at time t interpolated using the blended two-body motion propagation approximation

$\overline{\boldsymbol{P}}_j^{I}(t,e)$ = position-velocity covariance of the jth satellite at time t interpolated using the two-body motion propagation approximation from the eth tabulated ephemeris time

$\overline{\boldsymbol{P}}_{j,e}$ = eth ephemeris mean position-velocity state covariance for the jth satellite

$\overline{\boldsymbol{P}}_{j,t}$ = covariance matrix of the position-velocity state for the jth satellite at time t

$\widetilde{\boldsymbol{P}}_{j,t}$ = effective covariance of the position-velocity vector of the jth satellite at time t, adjusted to account for curvilinear trajectory effects

$\widetilde{\boldsymbol{P}}_t$ = effective covariance of the relative primary-to-secondary position-velocity vector, adjusted to account for curvilinear trajectory effects

$p_{a,k}$ = statistical t-test significance probability for the ascending portion of the kth collision rate peak

$p_{b,k}$ = statistical t-test significance probability for the descending portion of the kth collision rate peak

$\boldsymbol{Q}_j(t, t_{j,0})$ = process noise-type matrix applied to the propagated covariance $\overline{\boldsymbol{P}}_{j,t}$

$\boldsymbol{q}_{j,e}$ = eth ephemeris attitude quaternion vector for the jth satellite

R = $R_1 + R_2$ equals the combined primary and secondary hard-body radii

R_j = hard-body radius of the jth satellite

$\mathcal{R}_t(\hat{\boldsymbol{r}}')$ = the distance to the collision hull's surface, measured from the origin of the primary satellite's reference frame along the radial direction $\hat{\boldsymbol{r}}'$

$\overline{\boldsymbol{r}}_j^{\mathrm{BH}}(t)$ = mean position vector of the jth satellite at time t interpolated using the blended five-point Hermite method

$\overline{\boldsymbol{r}}_j^{H}(t,e)$ = mean position vector of the jth satellite at time t interpolated using the five-point Hermite method, centered on the eth tabulated ephemeris time

$\boldsymbol{r}_{j,t}$ = inertial-frame position vector of the jth satellite at time t

$\breve{\boldsymbol{r}}_{j,t}$ = effective mean of the position vector of the jth satellite at time t, adjusted to account for curvilinear trajectory effects

r_t = $|\boldsymbol{r}_t|$ equals the relative primary-to-secondary distance at time t

$\boldsymbol{r}_t$ = $\boldsymbol{r}_{2,t} - \boldsymbol{r}_{1,t}$ equals the relative primary-to-secondary position vector at time t

$\breve{\boldsymbol{r}}_t$ = effective mean of the relative primary-to-secondary position vector at time t, adjusted to account for curvilinear trajectory effects

$\hat{\boldsymbol{r}}$ = radial unit vector; $[\cos(\phi)\sin(\theta), \sin(\phi)\sin(\theta), \cos(\theta)]^T$

$\hat{\boldsymbol{r}}'$ = radial unit vector in the primary satellite's reference frame

$\boldsymbol{S}_{j,0}$ = orbital state vector at the initial time for the jth satellite, a random variable in this formulation

$\overline{\boldsymbol{S}}_{j,0}$ = mean orbital state at the initial time for the jth satellite

$\boldsymbol{S}_0$ = initial joint primary and secondary satellite orbital state vector, is a random variable in this formulation

T = time of closest approach

$T_{a,k}$ = begin time of the kth relative distance encounter segment which contains the kth conjunction

$\mathbb{T}_{a,k}$ = begin time of the kth collision rate encounter segment

$T_{b,k}$ = end time of the kth relative distance encounter segment which contains the kth conjunction

$\mathbb{T}_{b,k}$ = end time of the kth collision rate encounter segment

T_k = time of closest approach (minimum relative distance) for the kth conjunction

$\mathbb{T}_k$ = time of peak collision rate for the kth collision rate encounter segment

t = time

$t_{j,e}$ = eth ephemeris time for the jth satellite, with e equal to $1, \ldots, N_j^e$

$t_{j,0}$ = initial time (or orbit determination solution epoch) for the jth satellite

$\mathfrak{t}_{m,i}$ = time of the ith ingress during the mth Monte Carlo trial

t' = alternate time variable

$U(x)$ = unit-step function for the scalar quantity x; $U(x)$ equals 0 for $x \le 0$, and $U(x)$ equals 1 for $x > 0$

$\overline{\boldsymbol{v}}_j^{\mathrm{BL}}(t)$ = mean velocity vector of the jth satellite at time t interpolated using the blended five-point Lagrange method

$\overline{\boldsymbol{v}}_j^{L}(t,e)$ = mean velocity vector of the jth satellite at time t interpolated using the five-point Lagrange method, centered on the eth tabulated ephemeris time

$\boldsymbol{v}_{j,t}$ = inertial-frame velocity vector of the jth satellite at time t

$\breve{\boldsymbol{v}}_{j,t}$ = effective mean of the jth satellite velocity vector at time t, adjusted to account for curvilinear trajectory effects

$\breve{\boldsymbol{v}}_t$ = effective mean of the relative primary-to-secondary velocity vector at time t, adjusted to account for curvilinear trajectory effects

w_t = weight for blended ephemeris interpolation at time t

$\boldsymbol{\mathcal{X}}$ = $\boldsymbol{\mathcal{X}}(\boldsymbol{S}_{j,0}, t_{j,0}, t)$ is equal to the propagation function for the initial orbital state $\boldsymbol{S}_{j,0}$ [see Eq. (3)]

$\overline{\boldsymbol{X}}_{j,e}$ = eth ephemeris mean position-velocity state for the jth satellite

$\boldsymbol{X}_{j,t}$ = $\boldsymbol{X}_j(t)$ inertial-frame position-velocity vector of the jth satellite

$\breve{\boldsymbol{X}}_{j,t}$ = effective mean state of the position-velocity vector of the jth satellite at time t, adjusted to account for curvilinear trajectory effects

$\boldsymbol{X}_t$ = $\boldsymbol{X}_{2,t} - \boldsymbol{X}_{1,t}$ is equal to the relative primary-to-secondary position-velocity vector at time t

$\breve{\boldsymbol{X}}_t$ = effective mean state of the relative primary-to-secondary position-velocity vector at time t, adjusted to account for curvilinear trajectory effects

$[x]_+$ = $\max(0, x)$ is the nonnegativity operator for the scalar quantity x

$\boldsymbol{z}_t$ = example position vector specified in the inertial reference frame

$\boldsymbol{z}_t'$ = example position vector transformed into the primary satellite's reference frame

$\boldsymbol{\alpha}_t$ = two-body motion equinoctial-to-Cartesian orbital state transformation matrix

$\boldsymbol{\beta}_{t,t'}$ = two-body motion state transformation matrix for equinoctial states for propagation between times t and t'

$\Delta\widetilde{\mathcal{M}}_{R,t}(\hat{\boldsymbol{r}})$ = squared effective Mahalanobis distance function for a point on the collision sphere at time t, relative to the value at the center of the collision sphere

$\delta\dot{N}_{c,t}$ = approximated 1-sigma uncertainty on the collision rate at time t [see Eq. (32)]

$\delta(x)$ = unit-impulse function for the scalar quantity x
$\mathcal{E}_j$ = tabulated ephemeris for the jth satellite
θ = axial angle of the radial unit vector $\hat{\boldsymbol{r}}$
$\boldsymbol{\mu}_{p,t}$ = position vector of the peak overlap point at time t
$\nu()$ = average projected velocity function [see Eqs. (26) and (27)]
$\widetilde{\nu}$ = auxiliary quantity used to calculate average projected velocity function [see Eqs. (26) and (27)]
$\rho_{j,0}(\boldsymbol{S}_{j,0})$ = probability density function of the initial satellite orbital state vector $\boldsymbol{S}_{j,0}$
$\rho_0(\boldsymbol{S}_0)$ = probability density function of the initial joint orbital state vector $\boldsymbol{S}_0$
$\overline{\boldsymbol{\Sigma}}_{j,0}$ = covariance matrix of the orbital state at the initial time for the jth satellite
σ_v = auxiliary quantity used to calculate average projected velocity function [see Eqs. (26) and (27)]
τ_a = begin time for a risk assessment interval
τ_b = end time for a risk assessment interval
$\boldsymbol{\Phi}_{j,e,t}$ = two-body motion state transformation matrix for the jth satellite at time t for propagation from the eth tabulated ephemeris time
$\overline{\boldsymbol{\Psi}}_j(t, t_{j,0})$ = state transformation matrix propagating the covariance matrix $\overline{\boldsymbol{\Sigma}}_{j,0}$ from time $t_{j,0}$ to time t [see Eq. (6)]
ϕ = azimuthal angle of the radial unit vector $\hat{\boldsymbol{r}}$

I. Introduction

THE NASA Conjunction Assessment Risk Analysis (CARA) team estimates collision probabilities for a specific set of high-value Earth-orbiting satellites [1] based on the latest available satellite tracking data and orbit determination (OD) solutions [2]. Like many other organizations, CARA initially assesses collision risk using a *conjunction-by-conjunction* analysis method, a multistep process that first identifies close approach encounters (i.e., conjunctions) between two satellites, then calculates high-fidelity orbital states and associated covariance matrices at each time of closest approach (TCA), and finally estimates a collision probability P_c based on those TCA quantities. Given realistic trajectory uncertainty estimates, this approach is both efficient and accurate for typical interactions between near-Earth satellites. The computational efficiency results from the simplifying assumptions used by the single-conjunction P_c estimation methods. For instance, the commonly used 2D-P_c method uses rectilinear trajectories and neglects both velocity uncertainties and covariance temporal variations during encounters [3], assumptions appropriate for most high-velocity conjunctions. However, for lower-velocity interactions, these assumptions are not necessarily satisfied, so the approach potentially becomes inaccurate. Notably, even more advanced conjunction P_c estimation methods [4,5], which use two-body equations of motion to approximate encounter trajectories and covariance variations, potentially become inaccurate for highly extended interactions between closely orbiting objects, such as those experienced by tightly clustered satellites in geosynchronous orbit (GEO). Although these more challenging cases can be addressed using Monte Carlo (MC) estimation methods [6,7], the extended computations required for high-fidelity estimates can be prohibitive [8]. (See Ref. [9] for a recent review of P_c computation methods.)

Another disadvantage of the conjunction-by-conjunction method arises when analysts have access to state-covariance ephemeris tables for the two satellites but not a precalculated set of close approach events. In this case, applying the conjunction-by-conjunction method first requires finding all of the close approaches that occur, likely by using ephemeris interpolation combined with a numerical method to find the minima in the relative distance curve. This enables application of a single-conjunction P_c estimation method to each close approach event. However, after this, there remains the task of evaluating potential inaccuracies caused by ephemeris interpolation errors as well as the task of combining the results to estimate the cumulative risk for multi-encounter interactions.

This analysis formulates a method to estimate statistically expected collision rates and probabilities using only input ephemeris tables. The methodology differs significantly from the conjunction-by-conjunction approach. Specifically, the Eph-P_c method calculates the statistically expected collision rate as a continuous function of time throughout the risk assessment period and, from that, estimates P_c itself for isolated encounters, or establishes upper and lower P_c bounds for multi-encounter interactions. The algorithm accounts for both curvilinear trajectories and covariance evolution effects and provides estimates of uncertainties introduced by ephemeris interpolation inaccuracies. The ability to process irregularly sampled ephemerides allows application of the method to actively thrusting satellites. This entails using sufficiently short ephemeris time spacing throughout each thrusting event in order to resolve the resulting accelerations in time. Used in this way, the Eph-P_c method potentially enables safer operations for satellites that need to execute frequent or continuous translational maneuvers, such as those engaged in rendezvous and proximity operations with another satellite.

A. Objectives

This study primarily aims to formulate a semi-analytical method of calculating statistically expected collision rates and probabilities from orbital state/covariance ephemeris tables. Another objective is to use high-fidelity MC estimation [8] whenever possible to validate the accuracy of the P_c estimates. Auxiliary goals include applicability to all interactions experienced by near-Earth satellites (e.g., isolated high-velocity conjunctions or extended, low-velocity interactions), estimation of uncertainties caused by inaccurate interpolation or due to inadequately sampled ephemerides, and extension of the theory to account for object shape and attitude effects.

B. Methodology

The methodology differs from previous approaches in several fundamental ways. First, as mentioned previously, this formulation does not use a conjunction-by-conjunction P_c estimation approach. Instead, the Eph-P_c method employs a distinctly different multistep approach: first using state-covariance ephemeris interpolation to calculate the statistically expected collision rate as a continuous function of time $\dot{N}_c(t)$, then integrating over time to obtain the expected number of collisions N_c, and finally establishing upper and lower limits for the collision probability P_c.

The second way the methodology differs from most previous approaches is that it uses ephemeris interpolation to calculate the required orbital states and covariance matrices. Applying interpolation to irregularly sampled ephemerides enables application to thrusting objects and distinguishes the current methodology from other recent collision probability estimation approaches for long-term encounters [10–12]. This study specifically addresses the use of *Orbital Ephemeris Message* (OEM) tables, as defined by the Consultative Committee for Space Data Systems (CCSDS) [13]. The process requires an input OEM (or equivalent data structure) for each object, each tabulating Cartesian position-velocity (PV) states and associated covariance matrices, specified in an inertial reference frame (typically, the Earth-centered EME2000 frame [13,14]). As mentioned previously, the method allows nonuniform, asynchronous ephemerides. In other words, the two input ephemeris tables need not have uniform or matching temporal spacing. However, they must overlap somewhat in time. This overlap duration defines the maximum interval for risk assessment, an approach that prevents the need for extrapolation beyond the bounds of either ephemeris. The methodology estimates uncertainties caused by interpolation errors, which potentially can be large for inadequately sampled ephemerides.

The methodology also accounts for both the curvilinear nature of the satellite trajectories and the temporal evolution of the covariance matrices. Over time scales comparable to or longer than the ephemeris sampling intervals, the interpolation process itself accounts for the curvilinear trajectories and covariance evolution effects. Over shorter time scales, the formulation approximates these effects semi-analytically using two-body equations of motion.

Finally, in its most advanced form, the methodology also provides a semi-analytical means to account for the three-dimensional shape

Downloaded by 24.8.227.60 on February 14, 2025 | http://arc.aiaa.org | DOI: 10.2514/1.A36227

and attitude of the satellites. This enhancement requires ephemerides specifying time-dependent object orientations using attitude quaternions [15] and approximating shapes using convex hulls [16,17]).

C. Brief Outline of Paper

Section II reviews a selected set of established foundational concepts in order to provide context for the subsequent formulations. Section III describes ephemeris interpolation. Section IV derives the equations that the Eph-P_c method uses to estimate statistically expected collision rates and probabilities and describes the computational algorithm. Section V applies the Eph-P_c method to an illustrative set of actual near-Earth satellite interactions. Section VI compares the Eph-P_c analysis results to those generated by the conjunction-by-conjunction approach. Section VII discusses two advanced topics: accounting for satellite shape and attitude effects and estimating realistic collision rate and probability uncertainties. Readers interested primarily in the application of the Eph-P_c method should proceed directly to Secs. V and VI, skipping Secs. II–IV that focus on the formulation and algorithmic details.

II. Foundational Concepts

This section describes key concepts that provide foundational elements of the ephemeris-based formulation.

A. Orbit Determination Analysis and Initial Orbital States

An ephemeris used for near-Earth collision risk analysis tabulates high-fidelity trajectory predictions, propagated in time from an initial OD solution estimated from tracking measurements or other location data [2]. Each OD solution comprises a best-estimate (or mean) orbital state specified at an initial time (or epoch), along with a probability density function (PDF). Let $t_{1,0}$ and $t_{2,0}$ denote the OD epoch times for the primary and secondary satellites, respectively, or more generally $t_{j,0}$ with $j = 1$ or 2. This analysis denotes a mean OD epoch orbital state as $\overline{\boldsymbol{S}}_{j,0}$, which represents a real-valued column vector with dimension $N_j^S \times 1$. The PDF $\rho_{j,0}(\boldsymbol{S}_{j,0})$ represents the uncertainty of the OD solution, implicitly treating $\boldsymbol{S}_{j,0}$ as a random variable [18]. Ideally, the OD analysis would derive and report an accurate characterization of this PDF. However, OD state vector messages often only report an estimated covariance matrix $\overline{\boldsymbol{\Sigma}}_{j,0}$, which allows an approximation of the PDF in Gaussian form, expressed as a single multivariate normal (MVN) function

$$\rho_{j,0}(\boldsymbol{S}_{j,0}) \approx \mathcal{N}(\boldsymbol{S}_{j,0}, \overline{\boldsymbol{S}}_{j,0}, \overline{\boldsymbol{\Sigma}}_{j,0}) \tag{1}$$

with

$$\mathcal{N}(\boldsymbol{S}, \overline{\boldsymbol{S}}, \overline{\boldsymbol{\Sigma}}) = [\det(2\pi\overline{\boldsymbol{\Sigma}})]^{-1/2} \exp\left(-\frac{(\boldsymbol{S}-\overline{\boldsymbol{S}})^T\overline{\boldsymbol{\Sigma}}^{-1}(\boldsymbol{S}-\overline{\boldsymbol{S}})}{2}\right) \tag{2}$$

To improve uncertainty realism [19], advanced OD analyses could conceivably report a more accurate PDF as a *Gaussian mixture model* (GMM) distribution, that is, a weighted sum of multiple MVN functions [20,21]. In this case, the expressions presented in this study apply to each component arising from the GMM summations.

As in previous studies [4,7,8,22], this formulation employs an orbital state representation based on equinoctial orbital elements [23,24], decomposing the state vectors into two components, $\boldsymbol{S}_{j,0} = [\boldsymbol{E}_{j,0}^T \ \boldsymbol{b}_j^T]^T$, with $\boldsymbol{E}_{j,0}$ denoting the 6×1 vector of initial equinoctial elements and $\boldsymbol{b}_j$ denoting a vector of time-invariant auxiliary orbital state variables. For Earth-orbiting satellites, $\boldsymbol{b}_j$ often includes a ballistic coefficient and/or a solar radiation pressure parameter [8,14]. Notably, the choice of using equinoctial elements (specifically those based on mean motion and mean longitude) mitigates the impact of nonlinearities that cause inaccuracies in propagated uncertainties and covariances [7,22]. However, the equinoctial element processing software needs to account properly for potential singularities, such as for equatorial retrograde orbits [22–24].

B. High-Fidelity Orbital State Propagation and Covariance Propagation

OD states can be propagated using high-fidelity numerical integration to predict future inertial frame position-velocity states [2,14], represented in functional form as follows:

$$\boldsymbol{X}_j(t) = \boldsymbol{\mathcal{X}}(\boldsymbol{S}_{j,0}, t_{j,0}, t) \tag{3}$$

The function $\boldsymbol{\mathcal{X}}$ represents the nonlinear process that propagates with high accuracy the initial state $\boldsymbol{S}_{j,0}$ from the initial time $t_{j,0}$ to a future time t and then converts the result into a 6×1 PV state vector given by

$$\boldsymbol{X}_j(t) = \boldsymbol{X}_{j,t} = \begin{bmatrix} \boldsymbol{r}_{j,t} \\ \boldsymbol{v}_{j,t} \end{bmatrix} \tag{4}$$

where $\boldsymbol{r}_{j,t}$ and $\boldsymbol{v}_{j,t}$ denote the inertial-frame position and velocity vectors, respectively, for satellite j at time t. [Note that Eq. (4) introduces interchangeable subscript notation for the time variable, i.e., $\boldsymbol{X}_{j,t} = \boldsymbol{X}_j(t), \boldsymbol{r}_{j,t} = \boldsymbol{r}_j(t)$, etc., which is used for brevity throughout this formulation.] For near-Earth satellites, the propagation function $\boldsymbol{\mathcal{X}}$ also generally depends on a large ensemble of model and environmental data, such as Earth gravitational field coefficients and atmospheric density parameters [8].

The propagated PV covariance matrix $\overline{\boldsymbol{P}}_{j,t}$ can be estimated using nonlinear approaches (e.g., the MC method [25] or the polynomial chaos method [26]) or with linearized approximation as follows [2],

$$\overline{\boldsymbol{P}}_{j,t} \approx [\overline{\boldsymbol{\Psi}}_j(t, t_{j,0})]\overline{\boldsymbol{\Sigma}}_{j,0}[\overline{\boldsymbol{\Psi}}_j(t, t_{j,0})]^T + \boldsymbol{Q}_j(t, t_{j,0}) \tag{5}$$

with the state transition matrix (STM) comprising a $6 \times N_j^S$ matrix of partial derivatives,

$$\overline{\boldsymbol{\Psi}}_j(t, t_{j,0}) = \left(\frac{\partial \boldsymbol{\mathcal{X}}(\boldsymbol{S}_{j,0}, t_{j,0}, t)}{\partial \boldsymbol{S}_{j,0}}\right)_{\boldsymbol{S}_{j,0}=\overline{\boldsymbol{S}}_{j,0}} \tag{6}$$

The matrix $\boldsymbol{Q}_j(t, t_{j,0})$ improves covariance realism by accounting for errors in state modeling and propagation, which can be estimated as a process noise matrix [2], using an empirically calibrated state noise compensation technique [27,28], or through a consider parameter uncertainty analysis [29].

C. Orbital State and Covariance Ephemerides

An ephemeris in CCSDS OEM format [13] tabulates a set of time-ordered states and covariance matrices, represented by the set

$$\mathcal{E}_j = \{t_{j,e}, \overline{\boldsymbol{X}}_{j,e}, \overline{\boldsymbol{P}}_{j,e}\} \qquad e = 1 \ldots N_j^e \tag{7}$$

with $t_{j,e}$ indicating the eth ephemeris time, $\overline{\boldsymbol{X}}_{j,e} = \mathcal{X}(\overline{\boldsymbol{S}}_{j,0}, t_{j,0}, t_{j,e})$ indicating the associated propagated mean-state PV vector, and $\overline{\boldsymbol{P}}_{j,e}$ indicating the associated covariance matrix. The Eph-P_c method requires that the ephemerides for the primary satellite $\mathcal{E}_1$ and the secondary satellite $\mathcal{E}_2$ overlap one another, with the overlap bounded by the times $\tau_a = \max(t_{1,1}, t_{2,1})$ and $\tau_b = \min(t_{1,N_1^e}, t_{2,N_2^e})$, corresponding to the risk assessment interval, $\tau_a \le t < \tau_b$.

D. Circumscribing Spheres, Hard-Body Radii, and Convex Hulls

Because manufactured satellites generally have irregular shapes, most P_c methods estimate probabilities for collisions between spheres that circumscribe each of the two objects [30,31]. This hard-body radius (HBR) sphere parameterization is both conservative (because the spheres span each satellite's fully deployed components) and convenient (because each HBR is a single, time-invariant scalar). With this parameterization, collision rates and probabilities depend on the combined HBR of the primary and secondary satellites, $R = R_1 + R_2$.

If the satellite shapes are known, along with their time-dependent orientations, then it is possible to estimate somewhat smaller, refined P_c values, as has been discussed previously using an MC approach for high-velocity conjunctions [32] or a semi-analytical approach for

Downloaded by 24.8.227.60 on February 14, 2025 | http://arc.aiaa.org | DOI: 10.2514/1.A36227

Downloaded by 24.8.227.60 on February 14, 2025 | http://arc.aiaa.org | DOI: 10.2514/1.A36227

long-term encounters [33]. After first addressing the HBR parameterization, this study extends the formulation to account for shape and attitude effects. The semi-analytical formulation accounts for a satellite's shape using the convex hull parameterization [16].

E. Statistically Expected Collision Rates and Probabilities

As previously explained in detail [4], integrating over the joint uncertainty distribution of initial states provides a generalized method of estimating the statistically expected collision rate between satellites,

$$\dot{N}_{c,t} = \mathbb{E}[\dot{N}^D_{c,t}] = \int \rho_0(\boldsymbol{S}_0)\big[\dot{N}^D_c(\boldsymbol{X}_t(\boldsymbol{S}_0))\big]\,\mathrm{d}\boldsymbol{S}_0 \tag{8}$$

with the parts of this equation summarized as follows:

1) The symbol $\mathbb{E}$ denotes the expected value operator for interactions involving two satellites.

2) The symbol $\boldsymbol{S}_0$ represents the combined (or joint) OD initial state, $\boldsymbol{S}_0 = [\boldsymbol{S}^T_{1,0}\ \boldsymbol{S}^T_{2,0}]^T$.

3) The integral indicates integration over the entire domain of $\boldsymbol{S}_0$.

4) For statistically independent primary and secondary object OD orbital state distributions, the joint PDF is $\rho_0(\boldsymbol{S}_0) = \rho_{1,0}(\boldsymbol{S}_{1,0})\rho_{2,0}(\boldsymbol{S}_{2,0})$.

5) The function $\boldsymbol{X}_t(\boldsymbol{S}_0) = \boldsymbol{\mathcal{X}}(\boldsymbol{S}_{2,0}, t_{2,0}, t) - \boldsymbol{\mathcal{X}}(\boldsymbol{S}_{1,0}, t_{1,0}, t)$ represents the relative PV vector at time t, with dependence on the propagation epochs $t_{1,0}$ and $t_{2,0}$ suppressed for brevity.

6) The function $\dot{N}^D_{c,t} = \dot{N}^D_c(\boldsymbol{X}_t) = \delta(R^2 - |\boldsymbol{r}_t|^2)[-2(\boldsymbol{r}_t \cdot \boldsymbol{v}_t)]_+$ represents the *deterministic* collision rate, expressed as a function of the relative PV vector, $\boldsymbol{X}_t = [\boldsymbol{r}^T_t\ \boldsymbol{v}^T_t]^T$. In this expression, $\delta(x)$ denotes the unit-impulse (or Dirac delta) function [34,35], and $[x]_+ = \max(0, x)$ denotes the nonnegativity operator. The deterministic collision rate would be expected in the idealized absence of any tracking uncertainties or OD modeling errors, and the unit-impulse function reflects the discrete, instantaneous nature of ingress events between the two circumscribing spheres. (See Ref. [4] for a derivation of $\dot{N}^D_{c,t}$ from first principles.)

When applied to tracked satellites, the statistically expected collision rate in Eq. (8) varies as a function of time and typically peaks sharply at or near the TCA for isolated high-velocity conjunctions; for low-velocity interactions, the peaks have significantly longer durations and can occur farther from the close approach times. When applied to untracked satellites in nonresonant orbits around oblate central bodies, Eq. (8) yields semi-analytical expressions for long-term average collision rates [36] that are consistent with the method formulated in 1981 by Kessler [37].

For a specified risk assessment interval, $\tau_a \le t < \tau_b$, integrating the collision rate over time yields the statistically expected number of collisions

$$N_c = N_c(\tau_a, \tau_b) = \int_{\tau_a}^{\tau_b} \dot{N}_{c,t}\,\mathrm{d}t \tag{9}$$

The cumulative expected number of collisions during the interval, $N_{c,t} = N_c(\tau_a, t)$, is expressed similarly.

For tracked objects, the relationship between the statistically expected number of collisions and the collision probability is straightforward [4,5]. If the risk assessment interval $\tau_a \le t < \tau_b$ is shortened to include only one isolated encounter, then the two are equal: $N_c = P_c$. Longer-duration assessment intervals, such as the 7- or 10-day screening periods used by CARA, often contain several encounters (e.g., *repeating conjunctions* [38]). For a typical high-velocity multi-encounter interaction, the total expected number of collisions is the linear sum of the individual collision probabilities, that is, $N_c = \sum_k N_{c,k} = \sum_k P_{c,k}$, with the index k spanning all of the encounters. The total collision probability for a multi-encounter interaction has lower and upper limiting bounds $P^{\min}_c \le P_c \le P^{\max}_c$ given by [4,5]

$$\max_k(P_{c,k}) \le P_c \le 1 - \prod_k (1 - P_{c,k}) \tag{10}$$

The upper bound corresponds to full statistical independence between all of the encounters, and the lower bound represents the opposite extreme.

F. Monte Carlo Collision Probability Estimation

Equations (8) and (9) can be used to derive the cumulative statistically expected number of collisions estimated from a MC simulation [4], expressed as a summation of unit step functions

$$N^{\mathrm{MC}}_{c,t} = N^{\mathrm{MC}}_c(\tau_a, t) = \frac{1}{M}\sum_{m=1}^{M}\left[\sum_{i=1}^{I_m} U(t - \mathfrak{t}_{m,i})\right] \tag{11}$$

where the index $m = 1 \ldots M$ spans the MC trials and the set $\{\mathfrak{t}_{m,i}, i = 1 \ldots I_m\}$ represents the time-ordered ingress times during the mth trial, that is, the times that the spheres circumscribing the two satellites begin to overlap as they approach one another. [Note that the summation in the square brackets is defined to be zero if $I_m = 0$, meaning there are no ingresses for that trial. Also, the unit step function is defined as follows: $U(x) = 0$ for $x \le 0$ and $U(x) = 1$ for $x > 0$.] The expression for the cumulative collision probability $P^{\mathrm{MC}}_{c,t}$ is similar but includes only the first ingress that occurs per trial (if any occur) by including at most the first term in the square brackets in Eq. (11), yielding [4]

$$P^{\mathrm{MC}}_{c,t} = P^{\mathrm{MC}}_c(\tau_a, t) = \frac{1}{M}\sum_{m=1}^{M} U(t - \mathfrak{t}_{m,1}) \tag{12}$$

CARA's Brute Force Monte Carlo (BFMC) algorithm estimates multi-encounter collision probabilities using Eq. (12) combined with high-accuracy propagation to determine the ingress times for each MC trial [4,8]. This study uses BFMC to test the accuracy of the Eph-P_c method and refers to the first ingresses described previously as *hits*.

G. Conjunction-by-Conjunction Analysis

At this point, it is useful to review some of the key concepts used for conjunction-by-conjunction analysis, even though the Eph-P_c method does not use that approach. Conjunction-by-conjunction analysis entails a multistep process that first identifies close approach encounters between two satellites, then calculates high-fidelity states and covariance matrices at each TCA, and finally estimates collision probabilities based on those TCA quantities. CARA identifies close approaches using an efficient screening volume detection process that extends 7 or 10 days into the future, depending on the orbit of the primary object. Over such multiday screening periods, two objects may experience several close approaches, with TCA times given by the set $\{T_k, k = 1 \ldots K\}$. The processing system calculates the mean TCA position-velocity states $\overline{\boldsymbol{X}}_{j,T_k}$ using high-fidelity propagation and estimates the associated covariance matrices $\overline{\boldsymbol{P}}_{j,T_k}$. This produces a set of five quantities that characterize each conjunction, $\{T_k, \overline{\boldsymbol{X}}_{1,T_k}, \overline{\boldsymbol{P}}_{1,T_k}, \overline{\boldsymbol{X}}_{2,T_k}, \overline{\boldsymbol{P}}_{2,T_k}\}$, which are often stored and transmitted in the CCSDS Conjunction Data Message (CDM) format [39].

Each conjunction represents a local minimum in the mean relative distance curve, $\overline{r}_t = |\overline{\boldsymbol{r}}_{2,t} - \overline{\boldsymbol{r}}_{1,t}|$. The local minimum for the kth conjunction is bounded on either side by local maxima, spanning the interval $T_{a,k} \le t < T_{b,k}$. These conjunction time intervals represent *relative distance segments* (also known as *relative distance encounter segments* [4]) because they are defined using extrema of the $\overline{r}_t$ curve. Later, the formulation generalizes this concept to define two additional types of encounter segments: *Mahalanobis distance segments* and *collision rate segments*. (Note that this formulation often suppresses the index k when discussing single conjunctions or encounter segments.)

The CARA system and this study classify collision probabilities using a color-coded system: red conjunctions have $P_{c,k} \ge 10^{-4}$, yellow conjunctions have $10^{-7} \le P_{c,k} < 10^{-4}$, and green conjunctions have $P_{c,k} < 10^{-7}$.

Downloaded by 24.8.227.60 on February 14, 2025 | http://arc.aiaa.org | DOI: 10.2514/1.A36227

H. Single-Conjunction Analysis Using the Two-Body Motion Approximation

Single-conjunction methods estimate collision probabilities semi-analytically based on the primary and secondary states and covariances at the conjunction's close approach. More specifically, these methods calculate an approximation for P_c given the set $\{R, T, \overline{\boldsymbol{X}}_{1,T}, \overline{\boldsymbol{P}}_{1,T}, \overline{\boldsymbol{X}}_{2,T}, \overline{\boldsymbol{P}}_{2,T}\}$. The widely used 2D-$P_c$ single-conjunction method, originally formulated in 1992 by Foster and Estes [3] and later refined extensively [9,30,40–42], approximates the motion of each satellite during encounters using rectilinear trajectories. In 2021, Hall [4] developed the 3D-N_c method, which estimates conjunction P_c values using Kepler's two-body equations of motion to approximate encounter trajectories. Extensive MC testing indicates that, although the 2D-P_c and 3D-N_c methods produce effectively equivalent P_c estimates for the vast majority of CARA conjunctions (specifically those negligibly affected by curvilinear trajectory and covariance evolution effects), the 3D-N_c method provides significantly more accurate results for some events that involve low relative velocities, high eccentricity orbits, or long propagations [4,5,8].

The concepts and equations that underlie the semi-analytical 3D-N_c method also provide key foundational elements of the Eph-P_c formulation. The single-conjunction 3D-N_c method relies on two approximations. First, it approximates each satellite's equinoctial element state PDF at TCA as a Gaussian distribution, calculated using a single MVN function. Second, it uses two-body equations of motion over the duration of the encounter to approximate each satellite's trajectory, as propagated from the TCA. As mentioned previously, these approximations ultimately produce P_c values that accurately match the widely used 2D-P_c method for most CARA conjunctions. With these two approximations, Eq. (8) provides the means to derive a semi-analytical approximation for the collision rate during a conjunction. The straightforward but lengthy derivation (presented in detail in Ref. [4]) uses the combined primary and secondary TCA equinoctial states for the initial joint orbital state $\boldsymbol{S}_0$ and yields the following simplified expression:

$$\dot{N}_{c,t} \approx R^2 \int_0^{2\pi} \int_0^{\pi} \mathcal{F}_{t,T}(\phi, \theta, R) \sin(\theta)\, \mathrm{d}\theta\, \mathrm{d}\phi \tag{13}$$

Equation (13) represents integration over the surface of the collision sphere, which is centered on the primary satellite and has radius equal to the combined HBR, $R = R_1 + R_2$. The integrand function $\mathcal{F}_{t,T}(\phi, \theta, R)$, described in more detail later, depends on both the time of interest t and the TCA T. The azimuthal and axial angles ϕ and θ, respectively, span the sphere's surface, and the two associated integrals represent integration over the unit sphere. This study usually expresses the unit sphere integration in a more compact form,

$$\dot{N}_{c,t} \approx R^2 \oint \mathcal{F}_{t,T}(\hat{\boldsymbol{r}}, R)\, \mathrm{d}\hat{\boldsymbol{r}} \tag{14}$$

with the radial unit vector $\hat{\boldsymbol{r}} = [\cos(\phi)\sin(\theta), \sin(\phi)\sin(\theta), \cos(\theta)]^T$ measured from the mean position of the primary satellite and the integrand function expressed using the interchangeable notation $\mathcal{F}_{t,T}(\hat{\boldsymbol{r}}, R) = \mathcal{F}_{t,T}(\phi, \theta, R)$. The integrand function equals the product of an MVN function and an averaged projected velocity [4,43]:

$$\mathcal{F}_{t,T}(\hat{\boldsymbol{r}}, R) = \mathcal{N}(R\hat{\boldsymbol{r}}, \breve{\boldsymbol{r}}_t, \widetilde{\boldsymbol{A}}_t)\, \nu(R, \hat{\boldsymbol{r}}, \breve{\boldsymbol{X}}_t, \widetilde{\boldsymbol{P}}_t) \tag{15}$$

The 6×1 vector $\breve{\boldsymbol{X}}_t$ and associated 6×6 matrix $\widetilde{\boldsymbol{P}}_t$ represent the *effective* mean state and covariance of the relative PV vector, adjusted to account for curvilinear trajectory effects (as described in the next section), which are decomposed into position and velocity subcomponents as follows:

$$\breve{\boldsymbol{X}}_t = \begin{bmatrix} \breve{\boldsymbol{r}}_t \\ \breve{\boldsymbol{v}}_t \end{bmatrix} \quad \text{and} \quad \widetilde{\boldsymbol{P}}_t = \begin{bmatrix} \widetilde{\boldsymbol{A}}_t & \widetilde{\boldsymbol{B}}_t^T \\ \widetilde{\boldsymbol{B}}_t & \widetilde{\boldsymbol{C}}_t \end{bmatrix} \tag{16}$$

(Note that in Eqs. (13–16) the single-conjunction collision rate $\dot{N}_{c,t}$ as well as the quantities $\breve{\boldsymbol{X}}_t$ and $\widetilde{\boldsymbol{P}}_t$ also depend on the variable T, but this functional dependence is suppressed here for brevity.)

I. Curvilinear Motion Approximation Centered on Peak Overlap Position

Monte Carlo studies confirm that accounting for curvilinear trajectory effects involves accurately approximating the PDFs of the objects at the position where the two PDFs overlap the most [4]. Shelton and Junkins [44] introduced this concept in 2019 (specifically see the second figure of Ref. [44]), which was later developed into an iterative algorithm [4] that uses two-body equations of motion to estimate the peak overlap position (POP) of the two PDFs. The POP is a 3×1 position vector, denoted here as $\boldsymbol{\mu}_{p,t}$, that changes as a function of time during typical conjunctions. The converged POP calculation also provides the effective relative mean state, $\breve{\boldsymbol{X}}_t = \breve{\boldsymbol{X}}_{2,t} - \breve{\boldsymbol{X}}_{1,t}$, and associated covariance, $\widetilde{\boldsymbol{P}}_t = \widetilde{\boldsymbol{P}}_{1,t} + \widetilde{\boldsymbol{P}}_{2,t}$. (Note that this formula for $\widetilde{\boldsymbol{P}}_t$ assumes statistically independent primary and secondary PV states; see Ref. [4] for a discussion on how to account for nonindependent states).

III. Orbital State and Covariance Interpolation

The Eph-P_c method relies on interpolation to estimate orbital states and covariances between the discrete ephemeris points. This study uses ephemerides generated from Astrodynamics Support Workstation (ASW) orbit determination solutions [8], stored in CCSDS OEM text files using 16 digits of numerical precision [13]. This section describes the multipoint interpolation methods used for CARA's current implementation of the Eph-P_c algorithm. The algorithm uses different, customized interpolation methods for position vectors, velocity vectors, and covariance matrices.

A. Blended Five-Point Hermite Position Interpolation

Interpolating a mean position vector for satellite j at a time of interest t entails estimating the vector $\overline{\boldsymbol{r}}_j(t)$ from an ephemeris $\mathcal{E}_j$ of the form given in Eq. (7). This analysis interpolates each element of the position vector with the five-point Hermite method, which uses ephemeris positions and velocities to estimate intervening positions. (See Ref. [45] for a detailed description of multipoint Hermite interpolation.) To avoid discontinuities, the algorithm also employs a blending algorithm. Figure 1 illustrates the blended five-point interpolation concept, with the black circles representing the discrete ephemeris times $t_{j,e}$. In this case, the interpolation function plotted on the vertical axis of Fig. 1 represents one of the three scalar elements of $\overline{\boldsymbol{r}}_j(t)$. Let c indicate the index of the ephemeris point closest to the time of interest. If this coincides with the time of interest, then no interpolation is required. Otherwise, the process uses the five points $c-2, c-1, c, c+1, c+2$, as shown in Fig. 1. Applying Hermite interpolation to these five points yields the *closest-point* interpolant, which provides one approximation for the desired position, $\overline{\boldsymbol{r}}_j(t) \approx \overline{\boldsymbol{r}}_j^H(t, c)$. Unfortunately, this approximation can possess discontinuities at ephemeris midpoint times, where the closest index c abruptly

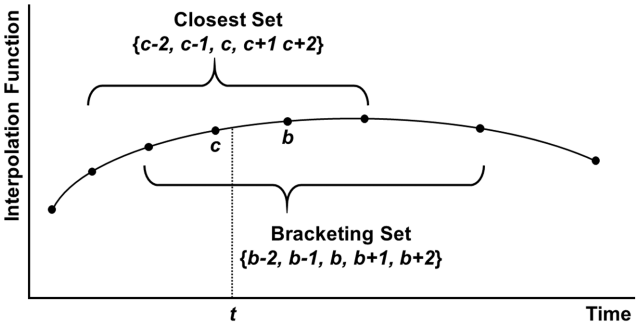

Fig. 1 The closest and bracketing ephemeris points (c and b, respectively) and associated five-point sets used for blended interpolation.

changes. A blending approach eliminates these discontinuities. Let b indicate the index that brackets the time of interest, as shown in Fig. 1, centered on the set $b-2, b-1, b, b+1, b+2$, which provides the *bracketing-point* interpolant $\overline{\boldsymbol{r}}_j^H(t,b)$. The blended five-point Hermite interpolant equals a weighted sum of the closest-point interpolant and the bracketing-point interpolant, as

$$\overline{\boldsymbol{r}}_j^{\mathrm{BH}}(t) = (1-w_t)[\overline{\boldsymbol{r}}_j^H(t,c)] + w_t[\overline{\boldsymbol{r}}_j^H(t,b)] \tag{17}$$

with the blending weight $w_t = (t-t_{j,c})/(t_{j,b}-t_{j,c})$ calculated from the closest and bracketing ephemeris times and restricted to the range $0 \le w_t \le 1$. The blended approximation $\overline{\boldsymbol{r}}_j(t) \approx \overline{\boldsymbol{r}}_j^{\mathrm{BH}}(t)$ does not change discontinuously at the ephemeris midpoints, or at any other times. However, the time derivatives of $\overline{\boldsymbol{r}}_j^{\mathrm{BH}}(t)$ can still possess discontinuities.

If the time of interest happens to be near either edge of an ephemeris, then the Eph-P_c algorithm shifts the five-point sets appropriately. For instance, if $c=1$ and $b=2$, then the shifted closest and bracketing five-point sets both become $\{1, 2, 3, 4, 5\}$. Experience indicates that such edge effects usually do not affect overall collision rates or probabilities significantly.

Similar shifting may also be required if an ephemeris contains one or more impulsive translational maneuvers, which can cause large and abrupt discontinuities in the tabulated quantities. In these cases, shifting the multipoint set prevents inappropriately interpolating across such discontinuities. A better approach for translational maneuvers, however, would be to create an ephemeris that resolves all of a satellite's accelerations in time by using sufficiently short time spacing throughout each thrusting event. This approach exploits the ability of the algorithm to process unevenly sampled ephemerides and allows estimation of collision rates and probabilities for thrusting satellites. Used in this way, the Eph-P_c method potentially enables safer operations for satellites that need to execute frequent or long-duration maneuvers. This initial study restricts analysis to ephemerides that contain no satellite translational maneuvers and defers for future studies further discussion of processing ephemerides that contain thrusting events.

B. Blended Five-Point Lagrange Velocity Interpolation

The current implementation of the Eph-P_c method interpolates each element of velocity vectors using the five-point Lagrange method. (See Ref. [46] for a detailed description of multipoint Lagrange interpolation.) As before, the five-point set centered on c yields the closest-point interpolant, $\overline{\boldsymbol{v}}_j(t) \approx \overline{\boldsymbol{v}}_j^L(t,c)$. The blended interpolant represents a weighted sum of the closest- and bracketing-point interpolants

$$\overline{\boldsymbol{v}}_j^{\mathrm{BL}}(t) = (1-w_t)[\overline{\boldsymbol{v}}_j^L(t,c)] + w_t[\overline{\boldsymbol{v}}_j^L(t,b)] \tag{18}$$

Again, this blended function does not possess discontinuities, but the time derivatives may.

C. Propagated and Blended Covariance Interpolation

Covariance interpolation entails estimating a symmetric, positive definite matrix $\overline{\boldsymbol{P}}_j(t)$ from an ephemeris $\mathcal{E}_j$ as given in Eq. (7), assumed here only to contain valid covariance matrices $\overline{\boldsymbol{P}}_{j,e}$ that are both symmetric and positive definite. Using the blended five-point Lagrange method for covariance interpolation often produces nonpositive definite (NPD) covariance matrices, especially for ephemerides involving long-duration propagations or high-eccentricity orbits. Using this approach would require that the Eph-P_c algorithm detect such NPD covariance matrices and remediate them to enable P_c estimation (see Ref. [47] for a discussion on NPD remediation). To avoid the creation of both NPD matrices and temporal discontinuities, this analysis interpolates covariances by blending the two covariance matrices propagated using the two-body motion approximation from the closest and bracketing ephemeris points.

Propagating the covariance matrix tabulated at the closest ephemeris time $\overline{\boldsymbol{P}}_{j,c}$, using the linearized approximation method provides the closest-point interpolant

$$\overline{\boldsymbol{P}}_j^I(t,c) = \boldsymbol{\Phi}_{j,c,t}\overline{\boldsymbol{P}}_{j,c}\boldsymbol{\Phi}_{j,c,t}^T \quad \text{with } \boldsymbol{\Phi}_{j,c,t} = \left(\frac{\partial \boldsymbol{X}_t}{\partial \boldsymbol{X}_{t_c}}\right)_{\overline{\boldsymbol{X}}_{j,c}} \tag{19}$$

The two-body motion STM $\boldsymbol{\Phi}_{j,c,t}$ can be calculated directly using Shepperd's method [48] or, equivalently, by using equinoctial elements and the chain rule to calculate the Jacobian matrix of partial derivatives, as

$$\frac{\partial \boldsymbol{X}_t}{\partial \boldsymbol{X}_{t_c}} = \left(\frac{\partial \boldsymbol{X}_t}{\partial \boldsymbol{E}_t}\right)\left(\frac{\partial \boldsymbol{E}_t}{\partial \boldsymbol{E}_{t_c}}\right)\left(\frac{\partial \boldsymbol{X}_{t_c}}{\partial \boldsymbol{E}_{t_c}}\right)^{-1} = \boldsymbol{\alpha}_t\boldsymbol{\beta}_{t,t_c}\boldsymbol{\alpha}_{t_c}^{-1} \tag{20}$$

with the two-body equinoctial-to-Cartesian transformation matrix $\boldsymbol{\alpha}_t$ given in the appendix of Ref. [49] and the relatively simple two-body STM for equinoctial states $\boldsymbol{\beta}_{t,t_c}$ given in Eq. (40) of Ref. [4]. Notably, as long as the STM $\boldsymbol{\Phi}_{j,c,t}$ has full rank and the ephemeris covariance matrices are valid, Eq. (19) cannot produce an asymmetric or NPD covariance matrix (at least to within the precision level of the computations).

Again, the blended covariance equals a weighted sum of the closest- and bracketing-point interpolants

$$\overline{\boldsymbol{P}}_j^{\mathrm{BI}}(t) = (1-w_t)[\overline{\boldsymbol{P}}_j^I(t,c)] + w_t[\overline{\boldsymbol{P}}_j^I(t,b)] \tag{21}$$

This weighted summation also cannot produce an asymmetric or NPD covariance matrix and yields temporal curves with no discontinuities (again, to within computational precision).

IV. Ephemeris-Based Collision Rate and Probability Estimation

The Eph-P_c method uses interpolated states and covariances to estimate the statistically expected collision rate between two objects as a function of time over the risk assessment interval $\tau_a \le t < \tau_b$ and then establishes upper and lower bounds for the accumulated collision probability. This section describes how the algorithm performs a relatively efficient initial search based on Mahalanobis distances to find approximate locations of peaks in the $\dot{N}_{c,t}$ curve, followed by an iterative method to subdivide the curve into encounter segments, integrating each using adaptive trapezoidal numerical integration [46], and finally applying Eq. (10) to estimate $P_c^{\min}$ and $P_c^{\max}$.

A. Statistically Expected Collision Rate

To estimate $\dot{N}_{c,t}$ values, the Eph-P_c method relies on slightly modified versions of the same two approximations used by the 3D-N_c method (see Sec. II.H). First, the formulation approximates each satellite's equinoctial state PDF as Gaussian in form *at all times during the risk assessment interval* (instead of only at conjunction TCAs). Second, it approximates each satellite's trajectory using two-body equations of motion *over POP-estimation time scales* (instead of over full conjunction durations). The first approximation allows the TCA T in the 3D-N_c method derivation to be replaced by the time of interest t. The second enables estimation of the POP, which requires approximating trajectories over time scales required for the objects to traverse distances comparable to $|\boldsymbol{\mu}_{p,t} - \overline{\boldsymbol{r}}_{j,t}|$. Combining these two modified approximations with Eq. (8) enables the derivation of the following simplified expression for $\dot{N}_{c,t}$ that, once again, represents an integral over the surface of the collision sphere:

$$\dot{N}_{c,t} \approx R^2 \oint \mathcal{F}_{t,t}(\hat{\boldsymbol{r}}, R)\, \mathrm{d}\hat{\boldsymbol{r}} \tag{22}$$

The derivation of this equation is almost identical to the lengthy formulation presented in Ref. [4], except with the variable T replaced with the variable t, and not repeated here. Expanding the integrand using Eq. (15) yields the final expression used by the Eph-P_c method to estimate statistically expected collision rates between the circumscribing spheres

Downloaded by 24.8.227.60 on February 14, 2025 | http://arc.aiaa.org | DOI: 10.2514/1.A36227

$$\dot{N}_{c,t} \approx R^2 \oint \mathcal{N}\left(R\hat{\boldsymbol{r}}, \breve{\boldsymbol{r}}_t, \widetilde{\boldsymbol{A}}_t\right) \nu\left(R, \hat{\boldsymbol{r}}, \breve{\boldsymbol{X}}_t, \widetilde{\boldsymbol{P}}_t\right) \mathrm{d}\hat{\boldsymbol{r}} \qquad (23)$$

As before, $\breve{\boldsymbol{X}}_t = \breve{\boldsymbol{X}}_{2,t} - \breve{\boldsymbol{X}}_{1,t}$ and $\widetilde{\boldsymbol{P}}_t = \widetilde{\boldsymbol{P}}_{2t} + \widetilde{\boldsymbol{P}}_{1,t}$ represent the effective mean and covariance of the relative PV vector, adjusted to account for curvilinear trajectory effects and decomposed into the subcomponents given by Eq. (16). The Eph-P_c method calculates $\breve{\boldsymbol{X}}_t$ and $\widetilde{\boldsymbol{P}}_t$ from a set of four interpolated quantities, $\{\overline{\boldsymbol{X}}_{1,t}, \overline{\boldsymbol{P}}_{1,t}, \overline{\boldsymbol{X}}_{2,t}, \overline{\boldsymbol{P}}_{2,t}\}$, using the same iterative POP-estimation algorithm described in detail in Ref. [4], again modified only by replacing T with t.

The collision rate given by Eq. (23) represents a continuous function of time. For instance, a low-velocity multi-encounter interaction might produce an $\dot{N}_{c,t}$ curve that contains a connected series of relatively wide peaks. However, high-velocity interactions typically produce a series of sharp peaks separated by intervals with $\dot{N}_{c,t} = 0$. Figure 2 illustrates these two types of interactions, based on 7 day ephemerides generated by the ASW system for actual Earth-orbiting satellites. The bottom panel plots rates for two closely orbiting GEO satellites experiencing several encounters, each with a very low relative speed of 0.04 m/s or less. (In 2019, Baars et al. [38] used the BFMC method to analyze this specific interaction.) The $\dot{N}_{c,t}$ curve in this case has a series of wide peaks and remains at nonzero levels throughout the interaction. The top panel of Fig. 2 plots rates for two low-Earth orbit (LEO) satellites encountering one another repeatedly at a much higher speed of 12.4 km/s. This produces a curve with a series of extremely short-duration peaks that occur about 2 days into the 7 day interval. These peaks have such short durations that they appear only as vertical lines in the top panel of Fig. 2. (For reference, Fig. 3 shows an expanded view of this sequence of peaks, and Fig. 4 shows a further expanded view of the tallest individual peak in the sequence.) Notably, a conjunction-by-conjunction analysis using the 2D-P_c method provides an accurate means to estimate the collision probability for this specific high-velocity interaction, producing results that match both the Eph-P_cP_c and BFMC methods, as discussed later. More generally, a multistep scheme that combines the 2D-P_c, 2D-N_c, and 3D-N_c methods [5] provides accurate results for the vast majority of CARA interactions; this multistep conjunction-by-conjunction algorithm is also significantly more efficient than

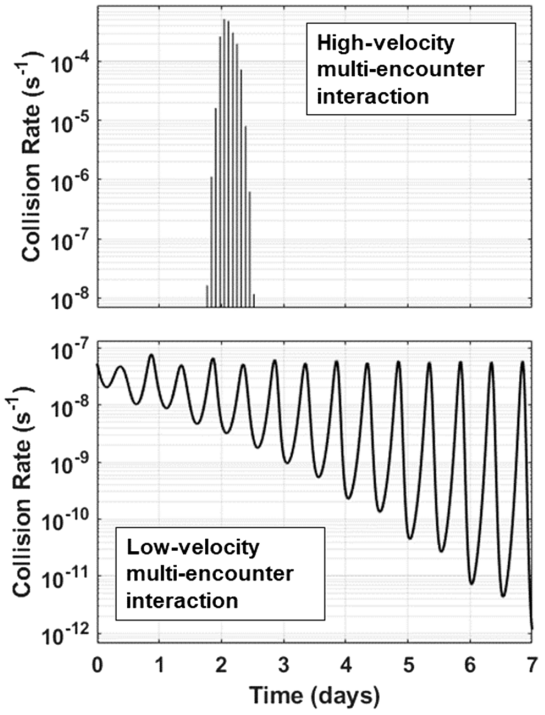

Fig. 2 Collision rate curves $\dot{N}_{c,t}$ for a high-velocity interaction between LEO satellites (top) and a low-velocity interaction between GEO satellites (bottom).

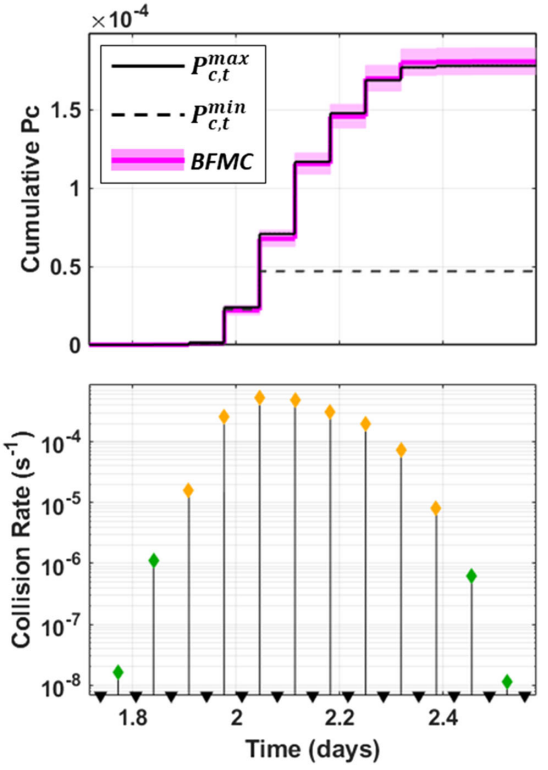

Fig. 3 Eph-P_c analysis of a high-velocity LEO satellite multi-encounter interaction, showing the collision rate (bottom) and cumulative collision probability (top).

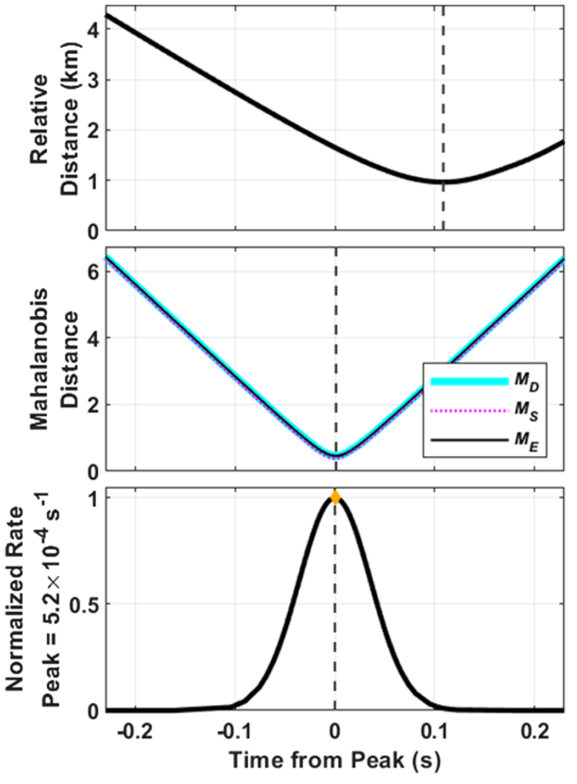

Fig. 4 Expanded view of the highest peak in Fig. 3, showing mean relative distance (top), Mahalanobis distances (middle), and $\dot{N}_{c,t}$ curve (bottom).

using the Eph-P_c method (at least as implemented for this study). The Eph-P_c method focuses on the kind of low-velocity interaction shown in the bottom panel of Fig. 2, for which the conjunction-by-conjunction approach can potentially be inaccurate. The next several

Downloaded by 24.8.227.60 on February 14, 2025 | http://arc.aiaa.org | DOI: 10.2514/1.A36227

sections describe how the Eph-P_c method calculates the statistically expected collision rate curves plotted in Fig. 2.

B. Collision Sphere Integral

Calculating a single $\dot{N}_{c,t}$ value with Eq. (23) entails evaluating a unit sphere integral, computed in this analysis with the Lebedev quadrature method [50] using the maximum available 5810 quadrature points. Each Lebedev quadrature point corresponds to a different $\hat{\boldsymbol{r}}$ vector, representing a different position on the unit sphere at which the integrand functions $\mathcal{N}(R\hat{\boldsymbol{r}}, \check{\boldsymbol{r}}_t, \widetilde{\boldsymbol{A}}_t)$ and $\nu(R, \hat{\boldsymbol{r}}, \check{\boldsymbol{X}}_t, \widetilde{\boldsymbol{P}}_t)$ must be computed.

The first integrand factor represents an MVN function, expressed as

$$\mathcal{N}(R\hat{\boldsymbol{r}}, \check{\boldsymbol{r}}_t, \widetilde{\boldsymbol{A}}_t) = \frac{e^{-\widetilde{\mathcal{M}}_{R,t}(\hat{\boldsymbol{r}})/2}}{(2\pi)^{3/2}|\widetilde{\boldsymbol{A}}_t|^{1/2}} \tag{24}$$

with $|\widetilde{\boldsymbol{A}}_t| = \det(\widetilde{\boldsymbol{A}}_t)$. The squared effective Mahalanobis distance for a point on the collision sphere is

$$\widetilde{\mathcal{M}}_{R,t}(\hat{\boldsymbol{r}}) = (R\hat{\boldsymbol{r}} - \check{\boldsymbol{r}}_t)^T\left[\widetilde{\boldsymbol{A}}_t^{-1}\right](R\hat{\boldsymbol{r}} - \check{\boldsymbol{r}}_t) \tag{25}$$

For brevity, this Mahalanobis distance function lists both R and t as subscript variables.

The second integrand factor $\nu(R, \hat{\boldsymbol{r}}, \check{\boldsymbol{X}}_t, \widetilde{\boldsymbol{P}}_t)$ represents an averaged projected velocity, originally derived in 2012 by Coppola [43] and later adapted to use POP linearization to account for curvilinear trajectory effects [4],

$$\nu\left(R, \hat{\boldsymbol{r}}, \check{\boldsymbol{X}}, \widetilde{\boldsymbol{P}}\right) = \frac{\sigma_v H(\widetilde{\nu})}{\sqrt{2\pi}} \text{ with } \sigma_v = \sqrt{\hat{\boldsymbol{r}}^T\left(\widetilde{\boldsymbol{C}} - \widetilde{\boldsymbol{B}}\widetilde{\boldsymbol{A}}^{-1}\widetilde{\boldsymbol{B}}^T\right)\hat{\boldsymbol{r}}} \text{ and} \tag{26}$$

$$H(\widetilde{\nu}) = e^{-\widetilde{\nu}^2} - \sqrt{\pi}\widetilde{\nu}\,\text{erfc}(\widetilde{\nu}) \text{ and } \widetilde{\nu} = \frac{\hat{\boldsymbol{r}} \cdot [\check{\boldsymbol{v}} + \widetilde{\boldsymbol{B}}\widetilde{\boldsymbol{A}}^{-1}(R\hat{\boldsymbol{r}} - \check{\boldsymbol{r}})]}{\sqrt{2}\sigma_v} \tag{27}$$

which uses the complementary error function, $\text{erfc}(\widetilde{\nu}) = 1 - \text{erf}(\widetilde{\nu})$.

For cases in which velocity uncertainties and position-velocity correlations are approximately negligible (i.e., if $\widetilde{\boldsymbol{C}}$ and $\widetilde{\boldsymbol{B}}$ are approximately zero), the velocity factor reduces to a simpler form, expressed compactly using the nonnegativity operator:

$$\nu\left(R, \hat{\boldsymbol{r}}, \check{\boldsymbol{X}}_t, \widetilde{\boldsymbol{P}}_t\right) \approx [-\hat{\boldsymbol{r}} \cdot \check{\boldsymbol{v}}_t]_+ \tag{28}$$

This approximation is nonzero only if the dot product $\hat{\boldsymbol{r}} \cdot \check{\boldsymbol{v}}_t$ is negative. This means that for negligible velocity uncertainties the unit-sphere integral of Eq. (23) reduces to a unit-hemisphere integral. The hemisphere corresponds to the half of the collision sphere facing the direction of the incoming secondary object. This unit-hemisphere integral can be transformed into an integral over a circular region on the plane perpendicular to the $\check{\boldsymbol{v}}_t$ vector. Notably, if trajectory curvature effects are also negligible, then $\check{\boldsymbol{v}}_t = \overline{\boldsymbol{v}}_t$, and this plane corresponds to the conjunction plane commonly used for 2D-P_c analysis [3,30,40–42].

C. Relationship Between Collison Rate and Mahalanobis Distance

For the Eph-P_c algorithm to integrate the collision rate over time, each peak of the $\dot{N}_{c,t}$ curve first must be located and then subdivided appropriately to allow accurate numerical integration. This analysis implements an initial search based on Mahalanobis distances to find approximate peak locations relatively efficiently, followed by an adaptive method to integrate the $\dot{N}_{c,t}$ curve numerically using the trapezoidal method [46].

To understand how Mahalanobis distances provide an efficient means to locate the $\dot{N}_{c,t}$ peaks, rewrite Eq. (25) in the form $\widetilde{\mathcal{M}}_{R,t}(\hat{\boldsymbol{r}}) = \widetilde{\mathcal{M}}_{0,t} + \Delta\widetilde{\mathcal{M}}_{R,t}(\hat{\boldsymbol{r}})$, which allows Eq. (23) to be rewritten as

$$\dot{N}_{c,t} \approx \frac{e^{-\widetilde{\mathcal{M}}_{0,t}/2}R^2}{(2\pi)^{3/2}|\widetilde{\boldsymbol{A}}_t|^{1/2}} \oint e^{-\Delta\widetilde{\mathcal{M}}_{R,t}(\hat{\boldsymbol{r}})/2}\,\nu\left(R, \hat{\boldsymbol{r}}, \check{\boldsymbol{X}}_t, \widetilde{\boldsymbol{P}}_t\right) \mathrm{d}\hat{\boldsymbol{r}} \tag{29}$$

The leading exponential factor involving $\widetilde{\mathcal{M}}_{0,t}$ typically dominates large-amplitude temporal variations, meaning that the $\dot{N}_{c,t}$ curve tends to have maxima near times that the $\widetilde{\mathcal{M}}_{0,t}$ curve has minima.

D. Finding Mahalanobis Distance Minima

Because calculating each $\widetilde{\mathcal{M}}_{0,t}$ value requires an iterative calculation to estimate the POP, for efficiency, the initial search process neglects trajectory curvature effects and instead finds minima of the squared mean Mahalanobis distance at the center of the collision sphere, $\overline{\mathcal{M}}_{0,t} = \overline{\boldsymbol{r}}_t^T\overline{\boldsymbol{A}}_t^{-1}\overline{\boldsymbol{r}}_t$. Extensive analysis conducted as part of this study confirms that, for both high- and low-velocity interactions, peaks in the $\dot{N}_{c,t}$ curve tend to occur near (but not exactly at) minima of the $\overline{\mathcal{M}}_{0,t}$ curve. Another function with minima that often occur even closer to the $\dot{N}_{c,t}$ peaks is the minimum squared mean Mahalanobis distance that occurs over the surface of the collision sphere

$$\overline{\mathcal{M}}_{\min,t} = \min_{\hat{\boldsymbol{r}}}\left[(R\hat{\boldsymbol{r}} - \overline{\boldsymbol{r}}_t)^T\overline{\boldsymbol{A}}_t^{-1}(R\hat{\boldsymbol{r}} - \overline{\boldsymbol{r}}_t)\right] \tag{30}$$

which can be approximated to first order in the quantity $R/|\overline{\boldsymbol{r}}_t|$ as

$$\overline{\mathcal{M}}_{\min,t} \approx \overline{\mathcal{M}}_{0,t} - 2R|\overline{\boldsymbol{A}}_t^{-1}\overline{\boldsymbol{r}}_t| \tag{31}$$

This approximation can become negative during very close approaches but still has minima that tend to align closely with collision rate maxima.

Calculating either $\overline{\mathcal{M}}_{0,t}$ or $\overline{\mathcal{M}}_{\min,t}$ requires significantly less computation than calculating $\dot{N}_{c,t}$ itself. For this reason, the Eph-P_c algorithm accurately refines the minima of both of these quantities before beginning the task of numerically integrating the $\dot{N}_{c,t}$ curve over time. First, the process uses an iterative bisection search [46] to find and refine all the local minima of $\overline{\mathcal{M}}_{0,t}$ within the entire risk assessment period. This step defines an initial grid of times based on the combined set of primary and secondary ephemeris points, then approximates $\overline{\mathcal{M}}_{0,t}$ at each grid time, and finally iteratively bisects grid intervals to locate the minima to within an absolute tolerance level of $\Delta\overline{\mathcal{M}}_{0,t} = 10^{-3}$. After convergence, the refined time grid typically possesses many increasingly finely spaced points surrounding each of the minima.

Next, the algorithm uses the same bisection search algorithm to find the minima of the $\overline{\mathcal{M}}_{\min,t}$ curve, which further refines the time grid. Testing indicates that this additional search improves the speed of the subsequent adaptive numerical integration of the $\dot{N}_{c,t}$ curve, which itself further refines the time grid (as described later).

As a final step, the algorithm performs a bisection search to find all of the $\overline{\mathcal{M}}_{0,t}$ maxima to within a relative tolerance level of $\Delta\overline{\mathcal{M}}_{0,t}/\overline{\mathcal{M}}_{0,t} = 10^{-3}$. Finding both the minima and the maxima in this manner provides the means to divide the risk assessment interval into Mahalanobis distance encounter segments, each containing one $\overline{\mathcal{M}}_{0,t}$ minimum bracketed by two maxima. For typical high-velocity multi-encounter interactions, these Mahalanobis distance segments coincide nearly identically with the relative distance segments that each contain one close approach (see Sec. II.G). For low-velocity interactions, however, these two types of encounter segments may differ significantly.

As discovered early in the development of the Eph-P_c algorithm, the multistep bisection search approach described previously does not work as well if the Mahalanobis distance curves possess abrupt discontinuities. This is the reason for implementing the blended interpolation methods described in Sec. III, which prevent discontinuities from occurring in the constituent quantities $\overline{\boldsymbol{r}}_t$ and $\overline{\boldsymbol{A}}_t$. Without such blended interpolation, the bisection searches can fail to converge or can find an unmanageably large number of small-amplitude local

Downloaded by 24.8.227.60 on February 14, 2025 | http://arc.aiaa.org | DOI: 10.2514/1.A36227

Downloaded by 24.8.227.60 on February 14, 2025 | http://arc.aiaa.org | DOI: 10.2514/1.A36227

extrema. With blended interpolation, the searches tend to converge stably, finding only the most relevant large-amplitude extrema.

E. Finding Collision Rate Maxima

The next step of the algorithm entails calculating $\dot{N}_{c,t}$ at each of the times in the refined grid and finding the maxima of the resulting $\dot{N}_{c,t}$ curve. For efficiency, the process assumes that $\dot{N}_{c,t} = 0$ for grid times with $\overline{\mathcal{M}}_{0,t} > 10^6$. For all other grid times, the process estimates $\dot{N}_{c,t}$ using Lebedev quadrature to approximate the unit-sphere integral in Eq. (29). As shown in Fig. 2, the resulting $\dot{N}_{c,t}$ curves typically possess large-amplitude variations corresponding to the sequence of encounters that occur during the interaction. However, because the process numerically approximates the $\dot{N}_{c,t}$ values, the curve also may possess multiple small-amplitude peaks, which tend to have short durations spanning relatively few time grid points. These small-amplitude peaks result from three numerical approximations: the iterative POP estimation (which only converges to a finite tolerance), Lebedev quadrature (which only approximates the unit sphere integral), and state/covariance interpolation (which can be inaccurate, especially for ephemerides with inadequate time sampling). To identify the small-amplitude maxima, the Eph-P_c algorithm compares the peak amplitudes to the combined uncertainties caused by these approximations. The first step of the process is to find all extrema that occur among the $\dot{N}_{c,t}$ values in the refined time grid, no matter how small the amplitude or short the duration. Let $\mathbb{T}_k$ represent the times that maxima in this initial set occur, with the $k = 1 \ldots K$ spanning all of the peaks found in the search. Let $\mathbb{T}_{a,k}$ and $\mathbb{T}_{b,k}$ denote the times of the minima bounding each of these maxima, such that $\mathbb{T}_{a,k} \le t < \mathbb{T}_{b,k}$ spans the full duration of each peak. As explained below, the algorithm uses an iterative process to identify the subset of these peaks that have small amplitudes and combines them with neighboring large-amplitude peaks. The process identifies small-amplitude peaks by comparing them to uncertainties introduced by the numerical approximations.

To estimate the uncertainties, the algorithm evaluates variations among a set of four alternate $\dot{N}_{c,t}$ estimates, calculated by combining the unblended interpolated states and covariances. As mentioned previously, the Eph-P_c method calculates individual $\dot{N}_{c,t}$ values using an input set of interpolated states and covariances, $\{\overline{\boldsymbol{X}}_{1,t}, \overline{\boldsymbol{P}}_{1,t}, \overline{\boldsymbol{X}}_{2,t}, \overline{\boldsymbol{P}}_{2,t}\}$. The blended interpolation process produces a unique set of such input states and covariances at each time, yielding the main estimate $\dot{N}^{(0)}_{c,t}$, which is the rate actually reported by the Eph-P_c algorithm and used to assess collision risk. To estimate the uncertainty on this quantity due to the numerical approximations, the algorithm uses the unblended state/covariance interpolants, of which two exist for each object. Combining these provides the means to calculate four alternate $\dot{N}_{c,t}$ estimates, which, in general, differ from both $\dot{N}^{(0)}_{c,t}$ and from one another. The first alternate $\dot{N}^{(1)}_{c,t}$ combines the primary object's closest-point state/covariance interpolants with the secondary's closest-point interpolants. The second $\dot{N}^{(2)}_{c,t}$ combines the primary's closest interpolants with the secondary's bracketing interpolants. The third and fourth combine the primary's bracketing interpolants with the secondary's closest and bracketing interpolants, respectively. The formulation estimates uncertainties using the unbiased variance [46] of these four alternate rates

$$(\delta\dot{N}_{c,t})^2 = \frac{1}{3}\sum_{i=1}^{4}\left(\dot{N}^{(i)}_{c,t} - \langle\dot{N}_{c,t}\rangle\right)^2 \tag{32}$$

with $\langle\dot{N}_{c,t}\rangle$ denoting the mean of the four rates and $\delta\dot{N}_{c,t}$ denoting the approximated 1-sigma uncertainty level. Small-amplitude peaks have magnitudes comparable to or smaller than this level of uncertainty.

To quantify the statistical significance of the peak that occurs at $t = \mathbb{T}_k$, the algorithm applies Student's statistical t test for significantly different means with unequal variances (see Ref. [46]). Comparing the peak rate to the preceding minimum rate (which occurs at $t = \mathbb{T}_{a,k}$) yields the t test significance probability for the ascending portion of the peak $p_{a,k}$. Very small $p_{a,k}$ values indicate the ascending portion has a statistically significant amplitude. The process evaluates the overall significance of the ascending portion using the following three-step test:

1) If the separation $\mathbb{T}_k - \mathbb{T}_{a,k}$ exceeds two time grid points, then the algorithm considers the ascending portion to be significant if $p_{a,k} < 0.05$.

2) If $\mathbb{T}_k - \mathbb{T}_{a,k}$ corresponds to a separation of two grid points, then the algorithm considers the ascending portion to be significant if $p_{a,k} < 0.01$.

3) If $\mathbb{T}_k - \mathbb{T}_{a,k}$ corresponds to a separation of only one grid point, then the algorithm considers the ascending portion to be significant if $p_{a,k} < 0.001$.

The process applies the same three-step test to the descending portion. The second and third steps require smaller significance probabilities for portions spanning only one or two grid intervals, which improves identification of short-duration low-amplitude peaks. If the tests find either the ascending or descending portions not to be significant, then the algorithm merges the identified low-amplitude peak with either the preceding or following peak. Repeating this process iteratively, starting with the least statistically significant peak, eliminates all of the low-amplitude maxima.

Notably, the iterative process does not neglect the low-amplitude peaks in the $\dot{N}_{c,t}$ curve; instead, it simply combines them with their larger amplitude neighbors but still fully includes their contribution to the expected number of collisions N_c and the collision probability limits $P_c^{\min}$ and $P_c^{\max}$. The converged peak-finding process subdivides the overall risk assessment interval, $\tau_a \le t < \tau_b$, into a set of collision rate segments, each containing one large-amplitude peak that occurs at $t = \mathbb{T}_k$, bracketed by minima that bound the kth collision rate segment which spans the interval $\mathbb{T}_{a,k} \le t < \mathbb{T}_{b,k}$. The segments abut one another with no gaps and cover the full risk assessment interval.

F. Adaptive Trapezoidal Integration of Collision Rate

The next step of the algorithm iteratively applies the trapezoidal numerical integration method [46] to estimate the expected number of collisions for each collision rate segment $N_{c,k}$ and for the total interaction, $N_c = \sum_k N_{c,k}$. The statistically expected collision for the kth rate segment is

$$N_{c,k} = \int_{\mathbb{T}_{a,k}}^{\mathbb{T}_{b,k}} \dot{N}_{c,t}\,\mathrm{d}t \tag{33}$$

The process approximates these integrals by applying the trapezoidal method to the unevenly spaced time steps from the refined grid. The first iteration uses the time grid as refined by the bisection searches for the Mahalanobis distance extrema. Subsequent iterations use the grid that has been refined further by the adaptive integration process itself.

Let $N_{c,k}(g)$ be the trapezoidal integration method contribution of the gth grid point to $N_{c,k}$. Similarly, let $N_c(g)$ be the gth contribution to N_c. To eliminate time steps that are too long, the process iteratively bisects the intervals on both sides of grid points that satisfy either of the following two conditions: $N_c(g)/N_c > 0.005$ or $N_{c,k}(g)/N_{c,k} > 0.05$. The first ensures that the full integration is accurate by preventing any single trapezoidal step from exceeding 0.5% of the total N_c value. The second ensures that the integration for each rate segment is reasonably accurate by preventing any step from exceeding 5% of the segment's $N_{c,k}$ value. The iterative bisection process continues until no grid points qualify for further bisection. After each iteration, the process updates the list of large-amplitude peaks using the t-test method. The converged $N_{c,k}$ and N_c estimates represent the statistically expected number of collisions for each segment and the full interaction, respectively.

G. Lower and Upper Collision Probability Bounds

At this point, the algorithm assumes that the expected number of collisions for each collision rate segment can be used as an approximation for the segment's collision probability, $P_{c,k} \approx N_{c,k}$. For

this approximation to be accurate, each segment's duration, $\mathbb{T}_{a,k} \leq t < \mathbb{T}_{b,k}$, must be short enough so that no repeated encounters occur within that isolated time interval. Extensive Monte Carlo testing studies indicate that collision rate segments for both high- and low-velocity interactions satisfy this assumption.

H. Evaluating Uncertainties due to Ephemeris Interpolation

Comparisons with BFMC simulations indicate that ephemerides with excessively long intervals between tabulated time points produce inaccurate collision rate and probability estimates. The alternate $N_{c,t}$ interpolants discussed in Sec. IV.E also provide a means to quantify these inaccuracies. Specifically, after convergence, the algorithm calculates the lowest and highest of the interpolants at each grid point: $\dot{N}_{c,t}^{\text{low}} = \min_i[\dot{N}_{c,t}^{(i)}]$ and $\dot{N}_{c,t}^{\text{high}} = \max_i[\dot{N}_{c,t}^{(i)}]$, with $i = 0 \ldots 4$. Integrating these two bounding curves over time provides bounds on the statistically expected number of collisions for the full interaction, $N_c^{\text{low}} \leq N_c \leq N_c^{\text{high}}$, as well as each encounter segment, $N_{c,k}^{\text{low}} \leq N_{c,k} \leq N_{c,k}^{\text{high}}$. This study quantifies the estimation accuracy for an entire interaction using a single scalar indicator,

$$\mathcal{A} = \max\left[\frac{N_c^{\text{high}} - N_c}{N_c}, \frac{N_c - N_c^{\text{low}}}{N_c}\right] \tag{34}$$

The accuracy indicator for the isolated kth segment $\mathcal{A}_k$ is defined similarly. Ephemerides with the default (or nominal) time spacing generated by the ASW-based system used in this study typically produce $\mathcal{A} < 1\%$, indicating a level of accuracy that is more than adequate for CARA risk assessments.

Analysis based on comparisons to high-fidelity BFMC estimates shows that, when defined in this manner, the accuracy indicator typically overestimates actual Eph-P_c method errors. For this reason, one should regard the indicator $\mathcal{A}$ as a conservative upper limit on the fractional uncertainty of the N_c and $P_c^{\max}$ estimates due to ephemeris interpolation errors and other numerical estimation inaccuracies. To detect inadequately sampled input ephemeris tables, an operational software implementation might check for indicators that are too large, perhaps issuing usage violation warnings for $\mathcal{A} > 5\%$ and usage violation errors for $\mathcal{A} > 20\%$. As discussed later, artificially degrading the sampling frequency of ASW-based ephemerides provides the means to study changes in these accuracy indicators.

I. Higher-Order Interpolation Methods

This formulation focuses on the specific five-point interpolation scheme described in Sec. III. Notably, the Eph-P_c algorithmic steps presented previously apply equally well to higher-order multipoint schemes or other interpolation methods. This includes blending interpolants to stabilize convergence as well as using unblended or alternate interpolants to evaluate uncertainties and detect inadequate ephemeris time sampling.

V. Application to Earth-Orbiting Satellite Interactions

This section applies Eph-P_c to actual interactions archived by the CARA organization, each selected to illustrate different aspects of the method. This includes an expanded discussion of the high- and low-velocity interactions plotted in Fig. 2, as well as a low-velocity LEO satellite interaction.

A. High Relative Velocity LEO Satellite Interaction

Figure 3 plots Eph-P_c results for the high-velocity (12.4 km/s) interaction shown previously in the top panel of Fig. 2. This example shows results calculated using ephemerides generated by the ASW-based system used for this study and for a combined HBR of $R = 20$ m. Processing the nominal ephemerides for the interaction shown in Fig. 3 indicates an expected number of collisions of $N_c = 1.78 \times 10^{-4}$ for the full interaction, with an ephemeris interpolation accuracy indicator of $\mathcal{A} = 0.20\%$. The bottom panel of Fig. 3 plots the collision rate restricted to the 1 day interval of highest risk. Once again, all of the individual peaks have such short durations that they appear only as vertical lines on the plot. (The bottom panel of Fig. 4 shows an expanded view of one of the peaks.) The bottom panel of Fig. 3 also marks the top of each peak with a color-coded symbol indicating the $P_{c,k}$ value: yellow diamonds mark peaks for encounter segments with $10^{-7} \leq P_{c,k} < 10^{-4}$, green diamonds mark peaks with $10^{-10} \leq P_{c,k} < 10^{-7}$, and downward-pointing triangles indicate peaks with $P_{c,k} < 10^{-10}$ that occur below the bottom axis. The top panel of Fig. 3 plots cumulative collision probability estimates, showing high-fidelity probabilities calculated using the BFMC simulation method and the bounding $P_{c,t}^{\min}$ and $P_{c,t}^{\max}$ curves calculated using the Eph-P_c method. BFMC indicates a final estimate of $P_c^{\text{MC}} = 1.81 \times 10^{-4}$, corresponding to 1809 hits out of 10,000,200 trials, with a 95% confidence interval (shown as the light pink band in Fig. 3) of 1.73×10^{-4} to 1.89×10^{-4}. (See Ref. [8] for more details on BFMC probabilities and confidence intervals.) Eph-P_c indicates an upper bound of $P_c^{\max} = 1.78 \times 10^{-4}$, statistically consistent with the BFMC estimate.

Figure 4 shows an expanded view of the peak with the highest $N_{c,k}$ value, which occurs just after two days into the 7 day risk assessment period. The bottom panel plots a normalized version of the collision rate, illustrating that this peak lasts only a fraction of a second, which is typical for such high-velocity interactions [8,51]. Processing the nominal ephemerides indicates $N_{c,k} = 4.7 \times 10^{-5}$ for this specific encounter segment, with an accuracy indicator of $\mathcal{A}_k = 0.074\%$. The vertical dashed line in the bottom panel of Fig. 4 marks the time of maximum $\dot{N}_{c,t}$, and the diamond plotted at the peak of the curve indicates a yellow-level collision probability. The top panel of Fig. 4 plots the mean primary-to-secondary distance curve $\overline{r}_t$ with the TCA marked using a vertical dashed line. The middle panel shows three Mahalanobis distance curves: the mean Mahalanobis distance at the center of the collision sphere, $M_D = (\overline{\mathcal{M}}_{0,t})^{1/2}$; the approximated minimum mean Mahalanobis distance over the collision sphere's surface, $M_S = ([\overline{\mathcal{M}}_{\min,t}]_+)^{1/2}$; and the effective Mahalanobis distance at the center of the collision sphere, $M_E = (\widetilde{\mathcal{M}}_{0,t})^{1/2}$, which accounts for curvilinear effects. The vertical dashed line in the middle panel marks the time of minimum M_D. A comparison of the vertical dashed lines in the three panels of Fig. 4 shows how collision rate maxima and Mahalanobis distance minima tend to align for such high-velocity interactions but tend to be offset somewhat from the TCA (as discussed in Refs. [4,5,8,43,51]).

The ASW-based system used in this study provides nominal primary and secondary object ephemerides that are synchronized (in that they both use the same time points), but with unequal point-to-point spacing (in this case, varying from 29.1 s down to 23.6 s over the 7 day interval shown in Fig. 3). To demonstrate how ephemeris time resolution affects estimation accuracy, this study artificially degrades the ephemerides by using only every nth tabulated time point. For instance, for $n = 2$, the degraded primary ephemeris uses the original odd-numbered points $\{1, 3, 5, \ldots\}$. If the secondary ephemeris were to use these same points, the two degraded ephemerides would remain synchronized. Instead, this study degrades the secondary ephemeris for $n = 2$ by using the even-numbered points $\{2, 4, 6, \ldots\}$. The process similarly interleaves points for higher values of n. This degradation approach produces both asynchronous and unevenly sampled primary and secondary ephemerides, which tests the ability of the software to process such inputs correctly. For the interaction shown in Fig. 3, processing the original nominal ASW ephemerides (corresponding to $n = 1$) produces an accuracy indicator of $\mathcal{A}(1) = 0.20\%$. Using $n = 2$ doubles the average interval between ephemeris times and produces $\mathcal{A}(2) = 0.42\%$. Doubling the interval several additional times (using $n = 4$, 8, 16, 24, and 32) yields $\mathcal{A}(4) = 0.74\%$, $\mathcal{A}(8) = 1.4\%$, $\mathcal{A}(16) = 3.2\%$, $\mathcal{A}(24) = 9.8\%$, and $\mathcal{A}(32) = 36\%$. This trend illustrates the sensitivity of the Eph-P_c method's estimation accuracy to the ephemeris sampling frequency for this interaction. In this case, $\mathcal{A}(n)$ increases nonlinearly for $n > 16$, which corresponds to an ephemeris time spacing exceeding 465 s. The other multi-encounter interactions discussed later show similar nonlinear growth with ephemeris time spacing. A more comprehensive future study, based on both actual and simulated data,

Downloaded by 24.8.227.60 on February 14, 2025 | http://arc.aiaa.org | DOI: 10.2514/1.A36227

would provide a better understanding of the method's performance in response to varying ephemeris sampling and other effects.

B. Low Relative Velocity GEO Satellite Interaction

Figure 5 uses the same format as Fig. 3 to show Eph-P_c results for the low-velocity (less than 0.04 m/s) interaction previously shown in the bottom panel of Fig. 2. This example uses a combined HBR of $R = 10$ m for the two GEO satellites. Processing the nominal ephemerides indicates $N_c = 9.05 \times 10^{-3}$ for the full interaction, with an accuracy indicator of $\mathcal{A} = 0.053\%$. The bottom panel of Fig. 5 plots the collision rate curve. The red diamonds indicate $P_{c,k} \geq 10^{-4}$ estimates for each of the encounter segments. The top panel of Fig. 5 plots the cumulative $P_{c,t}^{\min}$ and $P_{c,t}^{\max}$ curves, which bound the BFMC estimates. For the full interaction, BFMC yields $P_c^{\mathrm{MC}} = 8.11 \times 10^{-3}$ (4054 hits out of 5×10^5 trials) with a 95% confidence range of 7.86×10^{-3} to 8.36×10^{-3}. Eph-P_c indicates $P_c^{\max} = 9.01 \times 10^{-3}$, which exceeds the BFMC-P_c estimate by a statistically significant margin (as discussed in the next section).

Figure 6 shows an expanded view of the peak with the highest $N_{c,k}$ value, which occurs about 1 day into the 7 day risk assessment interval. The bottom panel plots a normalized version of the collision rate, illustrating that this individual $\dot{N}_{c,t}$ peak lasts about 12 h; this long duration results from the extremely low relative velocity of the two closely orbiting GEO satellites. Processing the nominal ephemerides indicates $N_{c,k} = 1.2 \times 10^{-3}$ for this single encounter segment, with an accuracy indicator of $\mathcal{A}_k = 0.12\%$. The vertical dashed line in the bottom panel marks the time of maximum $\dot{N}_{c,t}$, and the color-coded diamond indicates a red-level collision probability for the encounter segment. The top panel of Fig. 6 plots the relative distance with the vertical dashed line marking the nearest TCA. The middle panel shows the three Mahalanobis distance curves described previously with the vertical dashed line marking the time of minimum M_D. A comparison of the vertical dashed lines in the three panels of Fig. 6 shows a rough alignment of the times of the collision rate peak and Mahalanobis distance minimum, but a significant misalignment with the nearest TCA. In fact, in this case, the $\dot{N}_{c,t}$ peak counterintuitively aligns more closely with a maximum in the $\overline{r}_t$ curve. This indicates that, for such low-velocity encounters, minima in the $M_D = (\overline{\mathcal{M}}_{0,t})^{1/2}$ curve provide a significantly better indicator of peak rates than minima in the $\overline{r}_t$ curve.

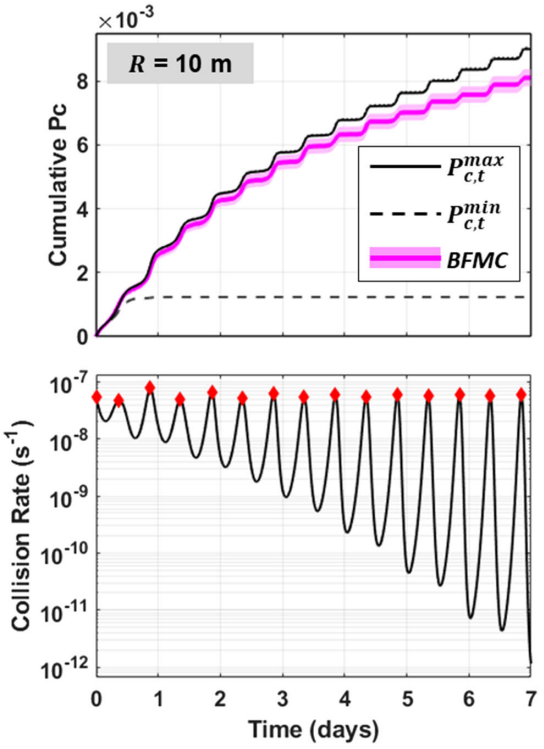

Fig. 5 Eph-P_c analysis of a low-velocity GEO satellite multi-encounter interaction, showing the collision rate (bottom) and cumulative collision probability (top).

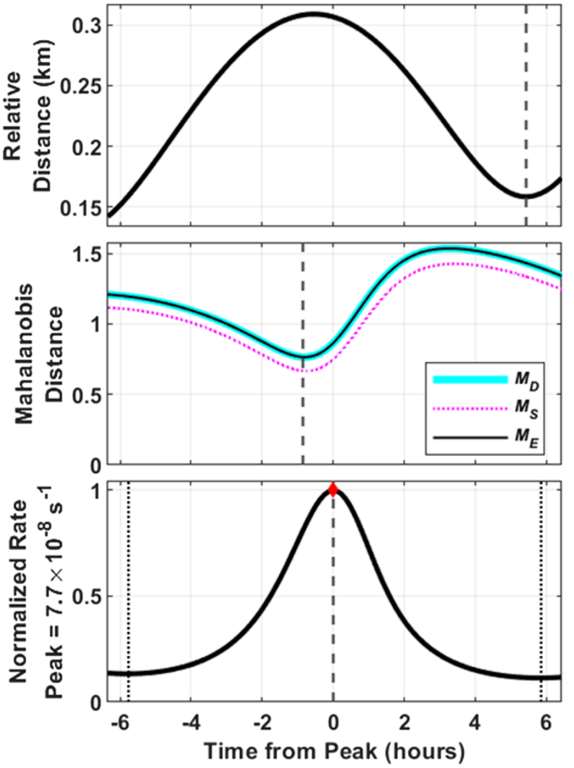

Fig. 6 Expanded view of the highest peak in Fig. 5, showing mean relative distance (top), Mahalanobis distances (middle), and $\dot{N}_{c,t}$ curve (bottom).

The nominal ASW-based primary and secondary object ephemerides for the interaction shown in Fig. 5 have time spacing that varies from 430 down to 379 s over the 7 day interval. As before, degrading the ephemerides by only using every nth tabulated point decreases the accuracy of the Eph-P_c results. The nominal ephemeris time spacing ($n = 1$) produces an accuracy indicator of $\mathcal{A}(1) = 0.053\%$. Repetitively doubling the average spacing indicates $\mathcal{A}(2) = 0.20\%$, $\mathcal{A}(4) = 7\%$, and $\mathcal{A}(8) = 190\%$, again indicating nonlinear sensitivity to sampling frequency.

C. Effects of Varying Hard-Body Radius

For most CARA multi-encounter interactions, the BFMC P_c^{MC} estimate and the $P_c^{\max}$ upper bound match one another to within MC statistical estimation uncertainty. This indicates that most CARA interactions have effectively statistically independent encounters. However, for the low-velocity GEO interaction shown in Fig. 5, the top panel clearly indicates that, for a combined HBR of $R = 10$ m, the BFMC P_c^{MC} estimate is somewhat lower than the $P_c^{\max}$ bound, that is, $P_c^{\mathrm{MC}}/P_c^{\max} \approx 0.90$. Figure 7 shows similar comparisons for the same interaction, but with the HBR decreased and increased by a factor of 10. The top panel of Fig. 7 plots cumulative probabilities for $R = 1$ m, which indicates statistically equivalent $P_c^{\max}$ and P_c^{MC} estimates. The bottom panel of Fig. 7 plots results for $R = 100$ m, which yields $P_c^{\mathrm{MC}}/P_c^{\max} \approx 0.58$. Increasing R from 1 to 100 m in this case clearly shifts the interaction from being a sequence of largely independent encounters, into a sequence of measurably nonindependent encounters.

For very small HBRs, essentially all of the collisions that occur at each encounter of this GEO interaction represent first contact collisions (see Sec. II.F). However, for very large HBRs, a significant number of collisions that occur during the later encounters represent second (or even higher) contacts; these contribute to the statistically expected number of collisions, but not to the collision probability, as indicated by Eqs. (11) and (12). The bottom panel of Fig. 7 clearly

Downloaded by 24.8.227.60 on February 14, 2025 | http://arc.aiaa.org | DOI: 10.2514/1.A36227

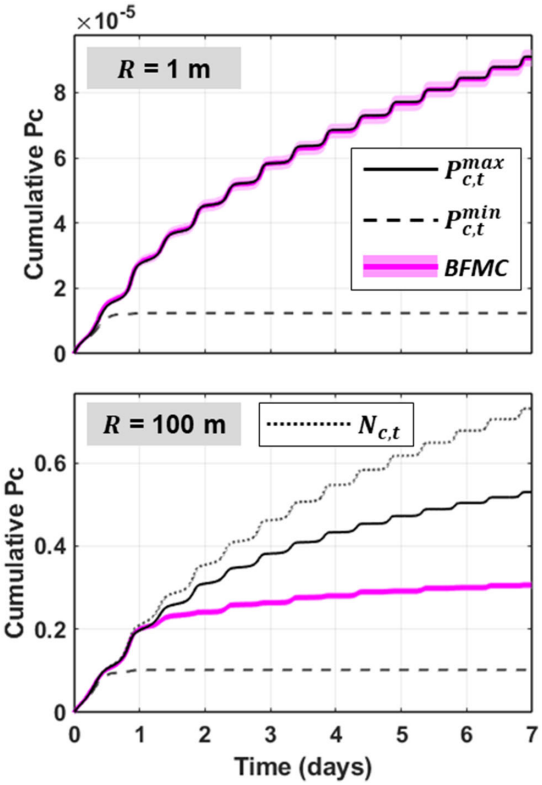

Fig. 7 Comparison of Eph-P_c and BFMC results for a low-velocity GEO interaction, for $R = 1$ m (top) and $R = 100$ m (bottom).

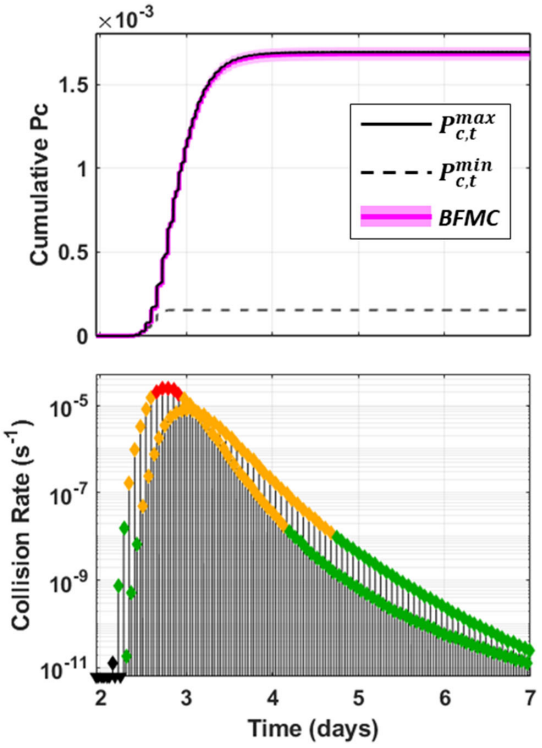

Fig. 8 Eph-P_c analysis of a low-velocity LEO satellite multi-encounter interaction, showing the collision rate (bottom) and cumulative collision probability (top).

shows this first contact effect, with the cumulative $P_{c,t}^{\mathrm{MC}}$ and $P_{c,t}^{\max}$ curves closely matching one another during the first day of the 7 day interaction but diverging increasingly thereafter. For reference, the bottom panel of Fig. 7 also plots the cumulative $N_{c,t}$ curve, clearly showing the inequality relationship $P_{c,t}^{\min} \le P_{c,t} \le P_{c,t}^{\max} \le N_{c,t}$.

Currently, the BFMC simulation method [8] provides the only means for CARA to estimate actual collision probabilities for multi-encounter interactions. CARA's semi-analytical methods technically only provide the means to estimate $P_c^{\min}$ and $P_c^{\max}$ bounds. As mentioned previously, most interactions analyzed with BFMC so far evidently have largely statistically independent encounters because in most cases the P_c^{MC} estimate and the $P_c^{\max}$ upper bound match one another. Exceptions to this tend to occur mostly for low-velocity interactions, especially those involving larger than average HBR values, as demonstrated in the bottom panel of Fig. 7. For high-velocity multi-encounter interactions, BFMC estimates tend to match $P_c^{\max}$ values even for large hard-body radii. For instance, for $R =$ 20 m, the high-velocity interaction shown in Fig. 3 has a $P_c^{\mathrm{MC}}/P_c^{\max}$ ratio statistically consistent with one (0.97 to 1.06 at 95% confidence, based on 1809 hits). Enlarging the HBR by a factor of 10 yields a $P_c^{\mathrm{MC}}/P_c^{\max}$ ratio also statistically consistent with one (0.984 to 1.014 at 95% confidence, based on 17,100 hits). So, even for $R = 200$ m, which is much larger than any current CARA-protected satellite, the individual encounters of the high-velocity interaction shown in Fig. 3 remain effectively statistically independent of one another to a high level of accuracy.

D. Low Relative Velocity LEO Satellite Interaction

Figure 8 shows Eph-P_c analysis results for a low-velocity interaction between two LEO objects, calculated using a combined HBR of $R = 10$ m. This interaction involves two newly colaunched satellites, inserted into similar orbits from the same upper stage. These encounter one another repeatedly during the 7 day risk assessment interval, with relative velocities varying in magnitude from 3.0 up to 354 m/s. Processing the nominal ASW-based ephemerides indicates $N_c = 1.69 \times 10^{-3}$ for the full interaction, with an accuracy indicator of $\mathcal{A} = 3.2\%$. The bottom panel of Fig. 8 plots the collision rate curve, again with color-coded symbols indicating segment $P_{c,k}$ magnitudes. The top panel plots the cumulative $P_{c,t}^{\min}$ and $P_{c,t}^{\max}$ curves, along with BFMC probabilities. For the full interaction, BFMC indicates $P_c^{\mathrm{MC}} = 1.68 \times 10^{-3}$ with a 95% confidence interval of 1.65×10^{-3} to 1.72×10^{-3} (based on 8404 hits). Eph-P_c indicates $P_c^{\max} = 1.69 \times 10^{-3}$, statistically consistent with the BFMC-P_c estimate.

Figure 9 shows an expanded view of the last red-level peak in the collision rate curve, which occurs about 3 days into the 7 day risk assessment interval. The bottom panel shows that this individual $\dot{N}_{c,t}$ peak lasts about 10 s, which is much longer than typical LEO conjunction durations [51]. Processing the nominal ephemerides indicates $N_{c,k} = 1.2 \times 10^{-4}$ for this single encounter segment, which has an accuracy indicator of $\mathcal{A}_k = 2.9\%$. The top panel of Fig. 9 plots the relative distance curve, indicating that the nearest TCA (not shown) is widely separated from the time of the collision rate peak. The middle panel shows the three Mahalanobis distance curves, with the vertical dashed line marking the time of minimum mean Mahalanobis distance M_D. Although the three Mahalanobis distance curves differ from one another significantly during this encounter segment, their minima collectively still provide a better indicator of the peak in collision rate than does the nearest minimum in the $\bar{r}_t$ curve.

The nominal ASW-based primary and secondary object ephemerides for the interaction shown in Fig. 8 have time spacing that varies between 27.8 down to 23.9 s over the 7 day interval. As before, degrading the ephemerides by only using every nth tabulated point decreases the accuracy of the Eph-P_c results. The nominal ephemeris time spacing ($n = 1$) produces Eph-P_c results with accuracy indicator of $\mathcal{A}(1) = 3.2\%$. Repetitively doubling the spacing indicates $\mathcal{A}(2) = 6.0\%$, $\mathcal{A}(4) = 12\%$, and $\mathcal{A}(8) = 22\%$.

E. Comparison to Brute Force Monte Carlo Method Collision Probabilities

The BFMC and Eph-P_c methods produce consistent collision probability estimates. More specifically, for sufficiently well-sampled ephemerides and sufficiently small HBR values, extensive comparisons

Downloaded by 24.8.227.60 on February 14, 2025 | http://arc.aiaa.org | DOI: 10.2514/1.A36227

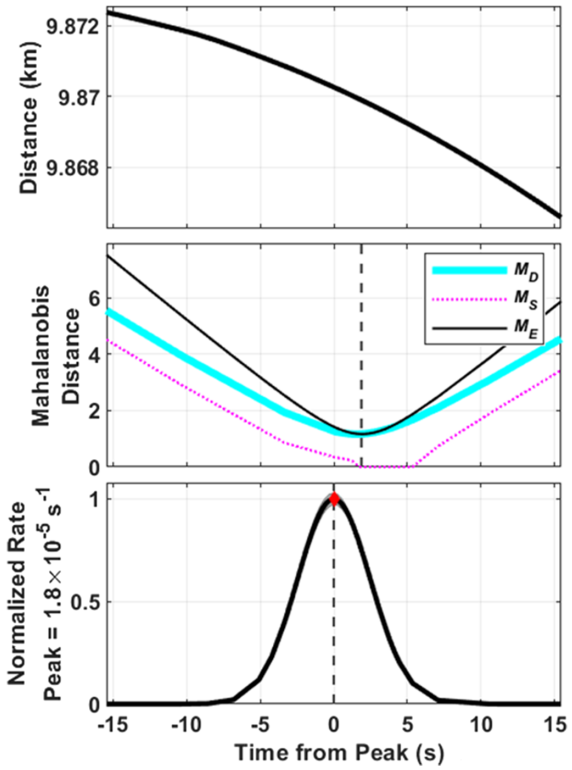

Fig. 9 Expanded view of the last red-level peak in Fig. 8, showing mean relative distance (top), Mahalanobis distances (middle), and $\dot{N}_{c,t}$ curve (bottom).

indicate no statistically significant differences between high-fidelity collision probabilities estimated using the BFMC method and the $P_c^{\max}$ upper bounds estimated using the Eph-P_c method. The top panels of Figs. 3, 7, and 8 graphically illustrate this agreement. Furthermore, larger HBR values yield BFMC estimates that satisfy the bounding relationship $P_c^{\min} \le P_c^{\mathrm{MC}} \le P_c^{\max}$ to within the MC uncertainties, as illustrated in the top panel of Fig. 5 and the bottom panel of Fig. 7. This consistency empirically validates the methods and approximations used in the Eph-P_c formulation.

BFMC repetitively samples equinoctial-based orbital states from single-Gaussian PDFs at the OD epoch times, propagates the sampled states over the risk assessment interval using high-accuracy ASW numerical integration, determines how many samples lead to hits, and finally estimates the probability as the number of hits divided by the number of samples. Eph-P_c estimates collision rates and probabilities using single-Gaussian equinoctial state PDFs estimated at each of the refined grid times within the risk assessment interval, with the required equinoctial state covariances calculated by transforming PV covariances interpolated from the ephemerides. These two methods would not produce consistent P_c estimates over such a wide range of interactions if using equinoctial orbital elements did not largely mitigate inaccuracies in propagated orbital state covariances. In summary, the agreement between Eph-P_c and BFMC estimates emphasizes the conclusion reached in previous studies that using equinoctial orbital elements mitigates the impact of nonlinearities that cause inaccuracies in propagated orbital state covariances [7,8,24,25].

VI. Comparison to Conjunction-by-Conjunction Estimation

A properly implemented conjunction-by-conjunction approach provides an accurate and efficient means to estimate collision probabilities for most interactions involving CARA-protected objects [5]. For these cases, the current Eph-P_c software implementation requires significantly more computation to obtain essentially equivalent results. In addition, the Eph-P_c algorithm is substantially more complex than single-conjunction estimation methods. This is why the Eph-P_c method focuses on the relatively infrequent low-velocity CARA interactions, for which the conjunction-by-conjunction approach may be inaccurate. Such inaccuracies can occur because conjunction-by-conjunction methods only employ TCA states and covariances, forcing them to approximate trajectories away from the TCA points semi-analytically using rectilinear or two-body equations of motion. Low relative velocities extend these simplified motion approximations over durations that are potentially too long for sufficiently accurate estimation. High-velocity interactions extend these motion approximations over much shorter time scales.

In 2023, Hall et al. [5] described a multistep conjunction-by-conjunction algorithm that accounts (if and when necessary) for curvilinear trajectories and covariance evolution effects using the two-body motion approximation. This multistep approach combines the increasingly accurate 2D-P_c, 2D-N_c, and 3D-N_c estimation methods and issues usage violation warnings for each if their required assumptions or approximations do not hold sufficiently. Most of these usage violations turn out to be false alarms because the criteria used to detect potential inaccuracies must be selected conservatively to reduce the rate of missed detections [5]. High-velocity conjunctions register usage violations least frequently. Altogether, roughly 5% of CARA conjunctions register usage violations for the 2D-P_c method (which uses the rectilinear motion approximation). A small fraction of these also register violations for the 2D-N_c method and, even less frequently, the 3D-N_c method (which both use the two-body motion approximation). Interactions that register usage violations for all three methods require follow-up processing using an alternative approach.

The conjunction-by-conjunction approach also can be inaccurate if the input set of TCA states and covariances is incomplete or, equivalently, if the input set of CDMs is incomplete. Each CDM represents an approach between the two satellites. A complete set corresponds to one CDM for each of the minima in the $\overline{r}_t$ curve. For efficiency, CARA initially identifies potentially high-risk conjunctions using a screening process, which creates a CDM data structure only if a close approach point also lies within a screening volume circumscribed around the primary object. (These volumes have either a box or ellipsoidal shape, aligned with the radial, in-track, cross-track reference frame directions; see Ref. [1] for a description of the CARA screening process). Although very efficient, this screening volume approach only captures a subset of the $\overline{r}_t$ minima, resulting in an incomplete set of CDMs. This incompleteness can lead to a moderate level of collision probability underestimation for some multi-encounter interactions.

A. High Relative Velocity LEO Satellite Interaction

For the high-velocity interaction shown in Fig. 3, high-fidelity ASW propagation [8] indicates that there are 205 minima in the $\overline{r}_t$ curve during the 7 day risk assessment interval. Applying the multistep conjunction-by-conjunction method [5] to all 205 indicates eight yellow-level and four green-level conjunctions, with the remaining 193 at lower P_c levels. For this interaction, the 2D-P_c, 2D-N_c, and 3D-N_c methods all yield equivalent results and register no usage violations. Combining the resulting P_c estimates using Eq. (10) yields $P_c^{\max} = 1.77\times10^{-4}$. This result is within 1% of the Eph-P_c estimate of $P_c^{\max} = 1.78\times10^{-4}$ generated using the nominal ASW-based ephemerides.

The CARA screening volume approach generates CDM data structures for the top five of the original 205 conjunctions (i.e., the five with the highest $P_{c,k}$ values). Together, these five indicate $P_c^{\max} = 1.66\times10^{-4}$, which is lower than the Eph-P_c estimate by about 7%.

B. Low Relative Velocity GEO Satellite Interaction

Applying the conjunction-by-conjunction approach to the low-velocity GEO interaction shown in Fig. 5 forces the multistep method [5] to use simplified equations of motion to approximate GEO trajectories over multihour intervals (more specifically, over TCA ± 6-h time scales, as indicated in the top panel of Fig. 6). Over such long durations, orbital perturbations (such as Earth's nonisotropic gravitational field, solar radiation pressure, or lunar and solar gravity

Downloaded by 24.8.227.60 on February 14, 2025 | http://arc.aiaa.org | DOI: 10.2514/1.A36227

Downloaded by 24.8.227.60 on February 14, 2025 | http://arc.aiaa.org | DOI: 10.2514/1.A36227

[14,15]) may have a nonnegligible effect on the trajectories, resulting in inaccurate collision probabilities. The analysis for $R = 1$ m shown in the top panel of Fig. 7 provides an example. High-fidelity ASW propagation [8] indicates that there are 14 minima in the $\overline{r}_t$ curve for this 7 day interaction. The CARA screening volume analysis generates CDM data structures for all 14. Applying the conjunction-by-conjunction approach using the 2D-P_c method registers multiple usage violations and yields $P_c^{\max} = 7.02 \times 10^{-5}$, which underestimates the Eph-P_c value of $P_c^{\max} = 9.10 \times 10^{-5}$ by about 33%. This is not surprising because the rectilinear motion approximation would not be expected to hold for the extended encounters that occur during this interaction. Using the 3D-N_c conjunction-by-conjunction method indicates $P_c^{\max} = 8.99 \times 10^{-5}$, which is 1.2% lower than the Eph-P_c value. However, the 3D-N_c method also registers multiple usage violations because the two-body motion approximation *potentially* could produce inaccurate results. In this case, these 3D-N_c usage violations essentially turn out to be false alarms. Nonetheless, the occurrence of such violations previously would have compelled a follow-up analysis using a computationally intensive BFMC simulation. The Eph-P_c method now provides a much more efficient, semi-analytical means of follow-up analysis in such cases.

C. Low Relative Velocity LEO Satellite Interaction

For the low-velocity LEO interaction shown in Fig. 8, high-fidelity ASW propagation [8] indicates that 111 minima occur in the $\overline{r}_t$ curve over the 7 day risk assessment interval. In this case, applying the conjunction-by-conjunction approach to all 111 using the 2D-P_c method yields $P_c^{\max} = 1.16 \times 10^{-3}$, which underestimates the Eph-P_c method estimate by 31%. Applying the 3D-N_c method to all 111 indicates $P_c^{\max} = 1.78 \times 10^{-3}$, which overestimates the Eph-P_c estimate by 5.3%. Again, the multistep analysis [5] registers multiple usage violations, compelling a follow-up analysis.

The 3D-N_c method indicates 75 of the 111 conjunctions have $P_{c,k} \geq 10^{-10}$. Notably, the Eph-P_c method indicates that 149 collision rate segments exceed this threshold (corresponding to the total number of peaks marked with green, yellow, and red diamonds in the bottom panel of Fig. 8). This means that each of the 75 conjunctions, on average, contains about two large-amplitude peaks in collision rate, a fact verified by a detailed comparison of the $\overline{r}_t$ and $\dot{N}_{c,t}$ curves for this interaction. More generally, multi-encounter interactions do not necessarily have one-to-one correspondence between close approaches and large-amplitude $\dot{N}_{c,t}$ peaks, especially for low relative velocities. In other words, the number of relative distance encounter segments does not necessarily equal the number of collision rate segments; in fact, for closely orbiting objects, the latter often outnumber the former by a factor of about 2. High-velocity interactions typically have a one-to-one correspondence between these two types of encounter segments. For instance, the high-velocity interaction shown in Fig. 3 has 12 $P_{c,k} \geq 10^{-10}$ conjunctions, with close approach times that occur relatively close to the 12 high-amplitude $\dot{N}_{c,t}$ peaks; moreover, the time intervals corresponding to the relative distance segments and collision rate segments over this 7 day high-velocity interaction are nearly identical.

The CARA screening volume approach generates CDM data structures for 20 of the original 111 conjunctions for the interaction shown in Fig. 8. Taken together, these 20 indicate $P_c^{\max} = 1.12 \times 10^{-3}$ using the 2D-P_c method and $P_c^{\max} = 1.53 \times 10^{-3}$ using the 3D-N_c method, which are 34 and 9.5% lower than the Eph-P_c estimate, respectively. Eight of the 111 original CDMs produce red-level $P_{c,k}$ values, but the screened CDMs include only seven of these. Similarly, 29 of the original 111 produce yellow-level $P_{c,k}$ values, but the screened CDMs include only 11 of these, meaning that the screening volume approach of detecting close approaches fails to detect over half of the yellow-level conjunctions for this interaction.

VII. Advanced Topics

This section discusses two advanced topics: extending the Eph-P_c method to account for satellite shape and attitude effects and a discussion of realistic collision rate and probability uncertainty estimation extending beyond the uncertainties due to ephemeris interpolation errors.

A. Accounting for Satellite Shape and Attitude Effects

The formulation presented so far estimates collision rates and probabilities for spheres that circumscribe each of the satellites. Accounting for satellite shape effects requires additional information and a generalization of some of the concepts. The additional information includes the convex hulls of the interacting satellites, along with their time-dependent orientations (i.e., attitudes).

This study specifies raw shape information using the vertex vectors for the satellite's main body and components, typically extracted from a CAD model. This set must include the vertices of all exterior components but optionally can include interior components as well. The set must also specify the vectors in the satellite's frame of reference, which often has an origin at the center of mass and has axes that rotate along with the main body. For satellites that have articulating (i.e., moving) components, a subset of these vertex vectors will depend on the articulation state of the satellite. The convex hull of the satellite is the smallest convex set that contains all of these vertices [16], computed as a subset of the original vertex vectors [17]. In other words, the hull is an irregular convex polyhedron that closely surrounds the satellite. The top panel of Fig. 10 shows the convex hull of the now-retired Cloud-Aerosol Lidar and Infrared Pathfinder Satellite Observations (CALIPSO) satellite [52], rendered as a semi-transparent surface around a CAD depiction. (More accurately, this surface represents the convex hull for one of the articulation states of the satellite.)

This study specifies time-dependent attitudes by adding quaternion vectors [15] to the ephemerides as follows:

$$\mathcal{E}_j = \{t_{j,e}, \overline{\boldsymbol{X}}_{j,e}, \overline{\boldsymbol{P}}_{j,e}, \boldsymbol{q}_{j,e}\} \quad e = 1 \ldots N_j^e \tag{35}$$

This formulation assumes that the quaternion vectors $\boldsymbol{q}_{j,e}$ have negligible uncertainties, although this assumption could be relaxed in future formulations. Interpolated quaternions $\boldsymbol{q}_{j,t}$ provide the means to compute the satellite's time-dependent attitude matrix, $\boldsymbol{a}_{j,t} = \boldsymbol{a}_f(\boldsymbol{q}_{j,t})$, where $\boldsymbol{a}_f$ represents the function that converts a 4×1 quaternion vector into the corresponding 3×3 attitude matrix. (See Ref. [15] for a description of quaternion vectors and attitude matrices.) Attitude matrices transform inertial-frame vectors into satellite-frame vectors. For instance, the following transformation converts the inertial-frame position $\boldsymbol{z}_t$ into the primary satellite's reference frame

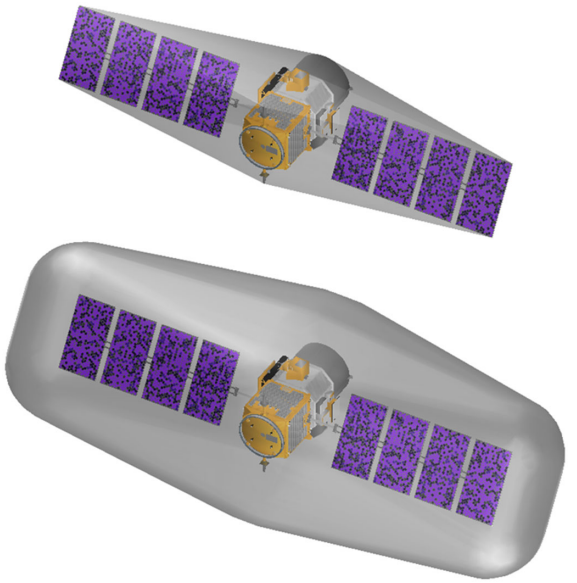

Fig. 10 Convex hull of CALIPSO satellite (top) and Minkowski sum of the convex hull and a sphere with a radius of 1 m (bottom).

$$\boldsymbol{z}_t' = \boldsymbol{a}_{1,t}(\boldsymbol{z}_t - \bar{\boldsymbol{r}}_{1,t}) \tag{36}$$

Attitude matrices also allow conversion of velocities and covariances into the primary's reference frame.

Including articulation state variables as part of the $\boldsymbol{q}_{j,e}$ ephemeris vectors provides the means to specify the overall orientation of a satellite and its moving parts. For instance, for a satellite with a solar panel assembly that rotates about a single axis, the $\boldsymbol{q}_{j,e}$ vector would include the panel rotation angle in addition to the four quaternion parameters that specify the orientation of the main body. Multiple moving parts require multidimensional articulation state vectors. An expanded convex hull that accounts for the full range of motion of each articulating component provides an alternative method to account for moving parts. This expanded hull always encompasses the satellite regardless of the articulation state that specifies the orientation of the moving parts. With this, the ephemeris $\boldsymbol{q}_{j,e}$ vectors need not include any articulation state parameters, but the resulting collision rates and probabilities will be increased somewhat due to the larger size of the hull.

Estimating the collision rate between the spheres circumscribing two satellites entails using Eq. (23) to calculate a unit sphere integral. Deriving the collision rate between two convex hulls also results in a unit sphere integral, but with a more complex integrand function,

$$\dot{N}_{c,t} \approx \oint [\mathcal{R}_t(\hat{\boldsymbol{r}}')]^2 \mathcal{F}_{t,t}(\hat{\boldsymbol{r}}', \mathcal{R}_t)\, \mathrm{d}\hat{\boldsymbol{r}}' \tag{37}$$

In this case, the integration is most conveniently performed in the primary satellite's reference frame, which has radial unit vector $\hat{\boldsymbol{r}}'$. As explained in more detail in the following paragraphs, the function $\mathcal{R}_t = \mathcal{R}_t(\hat{\boldsymbol{r}}')$ indicates the radial distance to the surface of the Minkowski sum [53–55] of the convex hulls of the primary and secondary objects. Deriving Eq. (37) uses the same assumptions and simplifications described previously, starting with the generalized expression given by Eq. (8), but using a deterministic collision rate function $\dot{N}_{c,t}^{D}$ that substitutes the $\mathcal{R}_t(\hat{\boldsymbol{r}}')$ function for R.

Replacing the integrand function $\mathcal{F}_{t,t}(\hat{\boldsymbol{r}}', \mathcal{R}_t)$ with $\mathcal{F}_{t,T}(\hat{\boldsymbol{r}}', \mathcal{R}_t)$ in Eq. (37) allows estimation for a single conjunction, with T representing the TCA. As before, if velocity uncertainties are negligible, then the unit sphere integral in Eq. (37) reduces to a unit-hemisphere integral; if trajectory curvatures are also negligible, then the unit-hemisphere integral can be transformed into a conjunction plane integral.

A Minkowski sum in three dimensions describes the convolved volume of two shapes and represents a fundamental operation for many modern applications including CAD modeling, assembly/disassembly planning, and robotic collision detection (see Refs. [53–55] and references therein for a description of Minkowski sums and their uses). For instance, the Minkowski sum of two spheres with radii R_1 and R_2 is another sphere with radius $R_1 + R_2$. The Minkowski sum of a cube and a much smaller sphere is a slightly larger cuboid shape, but with rounded corners and edges. In general, the Minkowski sum of two convex shapes produces another convex shape. If one of the two convex shapes is a sphere, then their Minkowski sum represents the surface traced out by the center of the sphere as it rolls over the entire surface of the other shape.

The bottom panel of Fig. 10 shows the Minkowski sum of CALIPSO's convex hull and a secondary sphere with radius $R_2 = 1$ m. (For reference, CALIPSO's central bus measures $1.5 \times 1.8 \times 2.3$ m and contains the origin of the satellite's reference frame.) In this case, the Minkowski sum produces an oblong convex shape, referred to here as the *collision hull*. Constructed in this manner, the collision hull always fits within the collision sphere, meaning that $\mathcal{R}_t(\hat{\boldsymbol{r}}') \leq R_1 + R_2$. In this regard, Eq. (37) represents an integral over the surface of the collision hull, whereas Eq. (23) represents an integral over the larger collision sphere. In both cases, Lebedev quadrature [50] provides an efficient method to calculate the required unit sphere integrals.

The function $\mathcal{R}_t(\hat{\boldsymbol{r}}')$ measures the distance from the origin along the direction $\hat{\boldsymbol{r}}'$ to the collision hull's surface. The convex shape of the collision hull ensures that $\mathcal{R}_t(\hat{\boldsymbol{r}}')$ is a single valued function. This enables the semi-analytical formulation and explains why the Eph-P_c method parameterizes satellite shapes using convex hulls. In general, the function $\mathcal{R}_t(\hat{\boldsymbol{r}}')$ depends on time due to changes in the relative attitudes of the two satellites and the motion of their articulating components. If the secondary's convex hull is a sphere with a time-invariant radius, then $\mathcal{R}_t(\hat{\boldsymbol{r}}')$ varies in time only if the primary satellite has actively articulating components. If the primary object is additionally a rigid body (or uses a static convex hull expanded to account for the full range of motion of each articulating component), then the resulting collision hull function does not vary in time.

In summary, Eq. (37) semi-analytically estimates statistically expected collision rates that incorporate shape and attitude effects, using as input the convex hull vertices and the attitude/articulation ephemerides. For multi-encounter interactions, the resulting $\dot{N}_{c,t}$ curve provides the means to estimate the expected number of collisions N_c and the upper-limit collision probability $P_c^{\max}$ using the same methodology described previously. Notably, the resulting $\dot{N}_{c,t}$ curve never exceeds the corresponding curve calculated using the full collision sphere, so incorporating shape and attitude effects generally reduces collision rate and probability estimates. The magnitude of the reduction depends on the relative sizes of the collision hull and the collision sphere. For interactions involving highly flattened or elongated satellites, the collision hull in many circumstances could be significantly smaller than the mostly empty collision sphere, leading to a substantial reduction. However, two relatively compact objects (such as a cubical primary and a spherical secondary), produce a collision hull that is only somewhat smaller than the collision sphere, likely leading to a more modest reduction. This means that assembling the required convex hull information and attitude/articulation ephemerides for relatively compact primary satellites may not be worth the effort. For satellites with large flat panels or long booms, the extra effort may be worthwhile because the reduced collision probabilities would less often exceed risk mitigation threshold values, thereby requiring fewer costly planned or executed collision risk mitigation maneuvers. Implementing this capability would also provide the means to assess the effectiveness of using only satellite attitude adjustments (rather than translational maneuvers) for collision risk mitigation. Attitude and shape processing also could be useful for planning low-risk satellite rendezvous and proximity operations.

B. Collision Rate and Probability Uncertainty Estimation

The Eph-P_c method accuracy indicator developed in Sec. IV.H evaluates uncertainties caused by ephemeris interpolation and other numerical inaccuracies in the computation. This accuracy indicator, however, does not measure the overall uncertainty of the risk assessment process. Realistic assessment of satellite collision risks requires accurate characterization of trajectory uncertainties. A 2016 review by Poore et al. [19] indicates that there are several sources of orbital state estimation errors, resulting in uncertainties due to random errors arising from natural variability, as well as uncertainties due to systematic errors arising from limited data or ignorance of physical processes. Covariances estimated for near-Earth satellites (and tabulated in ephemerides) often lack realism due to an incomplete accounting of these random and systematic OD uncertainties. Risk assessment based on collision probabilities implicitly assumes that the input covariances are realistic. Accounting for the lack of covariance realism alone leads to significant estimation uncertainties [56], which are likely much larger than those due to ephemeris interpolation (at least for the nominal ASW-based ephemerides used in this study).

Accounting fully for the lack of covariance realism and systematic OD errors may require using a combination of uncertainty analysis methods, such as those reviewed in 2013 by Zio and Pedroni [57]. In addition, several authors have identified concerns with the use of P_c itself as a risk assessment metric [58], including *diluted* probability [59], *false confidence* [60], and *statistically biased* estimation [61]. These and similar concerns have prompted the formulation of alternative methods and metrics for risk assessment and mitigation

Downloaded by 24.8.227.60 on February 14, 2025 | http://arc.aiaa.org | DOI: 10.2514/1.A36227

[62–64]. CARA continues to study these and other methodologies in order to assess collision risks reliably and estimate the associated uncertainties.

VIII. Conclusions

The Eph-P_c method uses orbital state and covariance ephemeris tables to estimate statistically expected collision rates and probabilities between Earth-orbiting satellites semi-analytically. The analysis shows that high-velocity interactions produce collision rate curves characterized by a series of short-duration peaks. Interactions with lower relative velocities produce peaks with longer durations. The other major conclusions are:

1) Numerically searching for minima in Mahalanobis distance curves provides an efficient means to find initial estimates for the times that peak collision rates occur.

2) Interpolating ephemerides using the blending method produces temporal curves without discontinuities and stabilizes the numerical searches.

3) Adaptive trapezoidal integration of the collision rate curve allows accurate computation of the statistically expected number of collisions, both for individual peaks in the rate curve and for the full interaction.

4) The accuracy indicator given by Eq. (34) provides a conservative upper limit on uncertainties caused by interpolation errors and provides the means to detect input ephemerides with inadequate time sampling.

5) The ability to process unevenly sampled ephemerides allows the Eph-P_c method to assess collision risks for satellites planning to execute frequent or continuous thrusting maneuvers; this requires ephemerides that use sufficiently short time spacing during thrusting events in order to resolve the resulting accelerations in time.

6) Accounting for satellite shapes and orientations requires ephemerides that tabulate attitude information and entails integration over the collision hull, calculated as the Minkowski sum of the two convex hulls.

Acknowledgments

NASA Goddard Space Flight Center funded this research through the "Flight Dynamics Support Services III" contract (contract number 80GSFC19C0072). The author would like to thank Luis Baars, Steve Casali, Todd Cerven, Joseph Frisbee, Matthew Hejduk, Dolan Highsmith, Nicolas Ravago, Daniel Snow, and Erick White for several helpful discussions and analyses.

References

[1] Newman, L. K., "The NASA Robotic Conjunction Assessment Process: Overview and Operational Experiences," *Acta Astronautica*, Vol. 66, Nos. 7-8, 2010, pp. 1253–1261. https://doi.org/10.1016/j.actaastro.2009.10.005.

[2] Tapley, B. D., Schutz, B. E., and Born, G. H., *Statistical Orbit Determination*, Elsevier Academic Press, Burlington, MA, 2004. https://doi.org/10.1016/b978-012683630-1/50020-5.

[3] Foster, J. L., and Estes, H. S., "A Parametric Analysis of Orbital Debris Collision Probability and Maneuver Rate for Space Vehicles," NASA TR JSC-25898, Aug. 1992.

[4] Hall, D. T., "Expected Collision Rates for Tracked Satellites," *Journal of Spacecraft and Rockets*, Vol. 58, No. 3, 2021, pp. 715–728. https://doi.org/10.2514/1.A34919.

[5] Hall, D. T., Baars, L. G., and Casali, S. J., "A Multistep Probability of Collision Computational Algorithm," *AAS Astrodynamics Specialist Conference*, AAS Paper 23-398, Springfield, VA, Aug. 2023.

[6] Alfano, S., "Satellite Conjunction Monte Carlo Analysis," *AAS Space-Flight Mechanics Meeting*, AAS Paper 09-233, Springfield, VA, Feb. 2009.

[7] Sabol, C., Binz, C., Segerman, A., Roe, K., and Schumacher, P. W., Jr., "Probability of Collisions with Special Perturbations Using the Monte Carlo Method," *AIAA/AAS Astrodynamics Specialist Conference*, AIAA Paper 2011-435, Aug. 2011.

[8] Hall, D. T., Casali, S. J., Johnson, L. C., Skrehart, B. B., and Baars, L. G., "High-Fidelity Collision Probabilities Estimated Using Brute Force Monte Carlo Simulations," *AAS Astrodynamics Specialist Conference*, AAS Paper 18-244, Springfield, VA, Aug. 2018.

[9] Li, J.-S., Yang, Z., and Luo, Y.-Z., "A Review of Space-Object Collision Probability Computation Methods," *Astrodynamics*, Vol. 6, No. 2, June 2022, pp. 95–120. https://doi.org/10.1007/s42064-021-0125-x

[10] Chan, K., "Elliptical Hovering Collision Probability for Long-Term Encounters," *AAS Astrodynamics Specialist Conference*, AAS Paper 21-604, Springfield, VA, Aug. 2021.

[11] Wen, C., and Qiao, D., "Calculating Collision Probability for Long-Term Satellite Encounters Through the Reachable Domain Method," *Astrodynamics*, Vol. 6, No. 2, June 2022, pp. 141–159. https://doi.org/10.1007/s42064-021-0119-8.

[12] Zollo, A., Parigini, C., Armellin, R., Diaz, J., and Kahle, R., "Long-Term Collision Probability Computation Through High-Order Taylor Polynomials Evaluation," *29th International Symposium on Space Flight Dynamics (ISSFD)*, April 2024.

[13] "Orbit Data Messages," *The Consultative Committee for Space Data System, Recommended Standard*, CCSDS 502.0-B-3, April 2023.

[14] Vallado, D. A., *Fundamentals of Astrodynamics and Applications*, 2nd ed., Microcosm Press, El Segundo CA, 2001.

[15] Wertz, J. R., *Spacecraft Attitude Determination and Control*, D. Reidel Publ., Dordrecht, Holland, 1978.

[16] Preparata, F. P., and Hong, S. J., "Convex Hulls of Finite Sets of Points in Two and Three Dimensions," *Communications of the ACM*, Vol. 20, No. 2, 1977, pp. 87–93. https://doi.org/10.1145/359423.359430.

[17] Barber, C. B., Dobkin, D. P., and Huhdanpaa, H., "The Quickhull Algorithm for Convex Hulls," *ACM Transactions on Mathematical Software*, Vol. 22, No. 4, 1996, pp. 469–483. https://doi.org/10.1145/235815.235821.

[18] Papoulis, A., and Pillai, S., *Probability, Random Variables, and Stochastic Processes*, 4th ed., McGraw Hill, New York, 2002, pp. 72–119.

[19] Poore, A. B., Aristoff, J. M., and Horword, J. T., "Covariance and Uncertainty Realism in Space Surveillance and Tracking, Defense Technical Information Center TR 1020892, June 2016.

[20] DeMars, K. J., Cheng, Y., and Jah, M. K., "Collision Probability with Gaussian Mixture Orbit Uncertainty," *Journal of Guidance, Control, and Dynamics*, Vol. 37, No. 3, 2014, pp. 979–985. https://doi.org/10.2514/1.62308

[21] Horwood, J. T., Aragon, N. D., and Poore, A. B., "Gaussian Sum Filters for Space Surveillance: Theory and Simulations," *Journal of Guidance, Control and Dynamics*, Vol. 34, No. 6, 2011, pp. 1839–1851. https://doi.org/10.2514/1.53793.

[22] Hernando-Ayuso, J., Bau, G., and Marinez-Cacho, A., "Near-Linear Orbit Uncertainty Propagation Using the Generalized Equinoctial Orbital Elements," *Journal of Guidance, Control and Dynamics*, Vol. 46, No. 4, 2023, pp. 654–665. https://doi.org/10.2514/1.G006864.

[23] Broucke, D. T., and Cefola, P. J., "On the Equinoctial Orbit Elements," *Celestial Mechanics*, Vol. 5, No. 3, May 1972, pp. 303–310. https://doi.org/10.1007/BF01228432

[24] Bau, G., Hernando-Ayuso, J., and Bombardelli, C., "A Generalization of the Equinoctial Orbital Elements," *Celestial Mechanics and Dynamical Astronomy*, Vol. 133, Nos. 11-12, 2021, pp. 1–29. https://doi.org/10.1007/s10569-021-10049-1

[25] Sabol, C., Sukut, T., Hill, K., Alfriend, K., Write, B., Li, Y., and Schumacher, P., "Linearized Orbit Covariance Generation and Propagation Analysis via Simple Monte Carlo Simulations," *AAS/AIAA Space Flight Mechanics Meeting*, AAS Paper 10-134, Springfield, VA, Feb. 2010.

[26] Jones, B. A., Doostan, A., and Born, G. H., "Nonlinear Propagation of Orbit Uncertainty Using Non-Intrusive Polynomial Chaos," *Journal of Guidance, Control and Dynamics*, Vol. 36, No. 2, 2013, pp. 430–444. https://doi.org/10.2514/1.57599

[27] Duncan, M., and Long, A., "Realistic Covariance Prediction for the Earth Science Constellation," *AIAA/AAS Astrodynamics Specialist Conference*, AIAA Paper 2006-6293, Aug. 2006. https://doi.org/10.2514/6.2006-6293.

[28] Zaidi, W. H., and Hejduk, M. H., "Earth Observing System Covariance Realism," *AIAA/AAS Astrodynamics Specialist Conference*, AIAA Paper 2016-5628, Sept. 2016. https://doi.org/10.2514/6.2016-5628.

[29] Cano, A., Pastor, A., Escobar, D., Miguez, J., and Sanjuro-Rivo, M., "Covariance Determination for Improving Uncertainty Realism in Orbit Determination and Propagation," *Advances in Space Research*, Vol. 72, No. 7, 2023, pp. 2759–2777. https://doi.org/10.1016/j.asr.2022.08.001

[30] Chan, K., *Spacecraft Collision Probability*, Aerospace Corp., El Segundo, CA. 2008. https://doi.org/10.2514/4.989186.

Downloaded by 24.8.227.60 on February 14, 2025 | http://arc.aiaa.org | DOI: 10.2514/1.A36227

[31] Mashiku, A. K., and Hejduk, M. D., "Recommended Methods for Setting Mission Conjunction Analysis Hard Body Radii," *AAS Astrodynamics Specialist Conference*, AAS Paper 19-702, Springfield, VA, 2019.

[32] de Vries, W. H., and Phillion, D. W., "Monte Carlo Method for Collision Probability Calculations Using 3D Satellite Models," *2010 AMOS Technical Conference*, Sept. 2010.

[33] Krier, G., "Satellite Collision Probability for Long-Term Encounters and Arbitrary Primary Satellite Shape," *Proceedings of 7th European Conference on Space Debris*, April 2017.

[34] Arfken, G. B., Weber, H. J., and Harris, F. E., *Mathematical Methods for Physicists*, 7th ed., Academic Press, New York, 2013, pp. 75–79. https://doi.org/10.1016/c2009-0-30629-7

[35] Dirac, P. A. M., *The Principals of Quantum Mechanics*, 4th ed., Oxford Univ. Press, Cambridge, MA, 1958, pp. 58–61.

[36] Hall, D. T., and Matney, M. J., "Collision Probabilities for Keplerian Orbits," *Space Debris*, Vol. 2, No. 3, Sept. 2000, pp. 161–198. https://doi.org/10.1023/A:1022916401768.

[37] Kessler, D. J., "Derivation of the Collision Probability Between Orbiting Objects: The Lifetimes of Jupiter's Outer Moons," *Icarus*, Vol. 48, No. 1, 1981, pp. 39–48. https://doi.org/10.1016/0019-1035(81)90151-2.

[38] Baars, L., Hall, D., and Casali, S., "Assessing GEO and LEO Repeating Conjunctions Using High Fidelity Brute Force Monte Carlo Simulations," *AAS Astrodynamics Specialist Conference*, AAS Paper 19-612, Springfield, VA, Aug. 2019.

[39] "The Consultative Committee for Space Data System, Conjunction Data Message," Recommended Standard, CCSDS 508.0-B-1, June 2013, with addendum Cor. 1, June 2018.

[40] Akella, M. R., and Alfriend, K. T., "The Probability of Collision Between Space Objects," *Journal of Guidance, Control, and Dynamics*, Vol. 23, No. 5, 2000, pp. 769–772. https://doi.org/10.2514/2.4611

[41] Alfano, S., "A Numerical Implementation of Spherical Object Collision Probability," *Journal of the Astronautical Sciences*, Vol. 53, No. 1, March 2005, pp. 103–109. https://doi.org/10.1007/BF03546397

[42] Elrod, C., "Computational Bayesian Methods Applied to Complex Problems in Bio and Astro Statistics,"Doctoral Dissertation, Baylor Univ, Waco, TX, July 2019.

[43] Coppola, V. T., "Including Velocity Uncertainty in the Probability of Collision Between Space Objects," *AAS/AIAA Spaceflight Mechanics Meeting,*, AAS Paper 12-247, Springfield, VA, Feb. 2012.

[44] Shelton, C. T., and Junkins, J. L., "Probability of Collision Between Space Objects Including Model Uncertainty," *Acta Astronautica*, Vol. 155, Feb. 2019, pp. 462–471. https://doi.org/10.1016/j.actaastro.2018.11.051

[45] Burden, R. L., and Faires, J. D., *Numerical Analysis*, 9th ed., Brookes/Cole, Boston, MA, 2011, pp. 136–142.

[46] Press, W. H., Teukolsky, S. A., Vettering, W. T., and Flannery, B. B., *Numerical Recipes in FORTRAN: The Art of Scientific Computing*, 2nd ed., Cambridge Univ. Press, New York, 1992.

[47] Hall, D. T., Hejduk, M. D., and Johnson, L. C., "Remediating Non-Positive Definite State Covariances for Collision Probability Estimation," *AAS Astrodynamics Specialist Conference*, AAS Paper 17-567, Springfield, VA, 2017.

[48] Shepperd, S. W., "Universal Keplerian State Transition Matrix," *Celestial Mechanics*, Vol. 35, No. 2, Feb. 1985, pp. 129–144. https://doi.org/10.1007/BF01227666

[49] Vallado, D., and Alfano, S., "Updated Analytical Partials for Covariance Transformations and Optimization," *AAS/AIAA Space Flight Mechanics Meeting*, AAS Paper 15-537, Springfield, VA, 2015.

[50] Lebedev, V., and Laikov, D., "A Quadrature Formula for the Sphere of the 131st Algebraic Order of Accuracy," *Doklady Mathematics*, Vol. 59, No. 3, 1999, pp. 477–481.

[51] Coppola, V. T., "Evaluating the Short Encounter Assumption of the Probability of Collision Formula," *AAS/AIAA Spaceflight Mechanics Meeting*, AAS Paper 12-248, Springfield, VA, Feb. 2012.

[52] Winker, D. M., Vaughan, M. A., Omar, A., Hu, Y., Powell, K. A., Liu, Z., Hunt, W. H., and Young, S. A., "Overview of the CALIPSO Mission and CALIOP Data Processing Algorithms," *Processing Algorithms, Journal of Atmospheric and Oceanic Technology*, Vol. 26, No. 11, 2009, pp. 2310–2323. https://doi.org/10.1175/2009JTECHA1281.1.

[53] Ruan, S., and Chirikjian, G. S., "Closed-Form Minkowski Sums of Convex Bodies with Smooth Positively Curved Boundaries," *Computer-Aided Design*, Vol. 143, Feb. 2022, Paper 103133. https://doi.org/10.1016/j.cad.2021.103133

[54] Li, W., "GPU-Based Computation of Voxelized Minkowski Sums with Applications," Doctoral Dissertation, UC Berkeley, Berkeley, CA, 2011.

[55] Cox, W., "A Review of Methods to Compute Minkowski Operations for Geometric Overlap Detection," *IEEE Transactions on Visualization and Computer Graphics*, Vol. 27, No. 8, 2021, pp. 3377–3396. https://doi.org/10.1109/TVCG.2020.2976922

[56] Hejduk, M. D., and Johnson, L. C., "Approaches to Evaluating Probability of Collision Uncertainty," *AAS Space Flight Mechanics Meeting*, AAS Paper 16-241, Springfield, VA, 2016.

[57] Zio, E., and Pedroni, N., Literature Review of Methods for Representing Uncertainty, *Cahiers de la Securte Industrielle*, Fondation pour une Culture de Securite Industielle, Toulouse France, 2013, http://www/FonCSI.org/fr/.

[58] Hejduk, M., and Snow, D., "Setting the Bar for the Replacement of the Probability of Collision Metric," *29th International Symposium on Space Flight Dynamics (ISSFD)*, April 2024.

[59] Alfano, S., "Relating Position Uncertainty to Maximum Conjunction Probability," *Journal of the Astronautical Sciences*, Vol. 53, No. 2, 2005, pp. 193–205. https://doi.org/10.1007/BF03546350

[60] Balch, M. S., Martin, R., and Ferson, S., "Satellite Conjunction Analysis and the False Confidence Theorem," *Proceedings of the Royal Society A: Mathematical, Physical and Engineering Sciences*, Vol. 475, No. 2227, 2019. https://doi.org/10.1098/rspa.2018.0565

[61] Elkantassi, S., and Davison, A. C., "Space Oddity? A Statistical Formulation of Conjunction Assessment," *Journal of Guidance, Control, and Dynamics*, Vol. 45, No. 12, 2022, pp. 2258–2274. https://doi.org/10.2514/1.G006282

[62] Sweetser, T. H., Braun, B. M., Acocella, M., and Vincent, M. A., "Quantitate Assessment of a Threshold for Risk Mitigation Actions," *Journal of Space Safety Engineering*, Vol. 7, No. 3, 2020, pp. 318–324. https://doi.org/10.1016/j.jsse.2020.07.009

[63] Modenini, D., Curzi, G., and Locarini, A., "Relations Between Collision Probability, Mahalanobis Distance, and Confidence Intervals for Conjunction Assessment," *Journal of Spacecraft and Rockets*, Vol. 59, No. 4, July 2022, pp. 1125–1134. https://doi.org/10.2514/1.A35234

[64] Delande, E. D., Jones, B. A., and Jah, M. K., "Exploring an Alternative Approach to the Assessment of Collision Risk," *Journal of Guidance, Control, and Dynamics*, Vol. 46, No. 3, 2023, pp. 467–482. https://doi.org/10.2514/1.G006709

R. Linares
Associate Editor

Downloaded by 24.8.227.60 on February 14, 2025 | http://arc.aiaa.org | DOI: 10.2514/1.A36227